Article | Open Access

Energy Materials

Chu et al. Energy Mater. 2026, 6, 600096 DOI:10.20517/energymater.2026.59

Design of quasi-solid-state electrolyte with continuous Li⁺ pathways via bridging cellulose and α-Li_2TiO_3 for lithium batteries

Dongxue Chu[1,2], Rui Gao[3,*], Linglong Hu[1], Hongji Xu[1], Daming Yang[1], Zhongjun Chen[4], Ze Gao[1], Wanxia Huang[4], Ming Feng[1,5,*]

Keywords:
Quasi-solid-state electrolyte, bridging effect, lithium dendrite, tip-shielding effect, lithium metal battery

Citation: Chu, D.; Gao, R.; Hu, L.; Xu, H.; Yang, D.; Chen, Z.; Gao, Z.; Huang, W.; Feng, M. Design of quasi-solid-state electrolyte with continuous Li⁺ pathways via bridging cellulose and α-Li_2TiO_3 for lithium batteries. *Energy Mater.* **2026**, *6*, 600096. https://dx.doi.org/10.20517/energymater.2026.59

Received: 8 Apr 2026 **First Decision:** 22 May 2026 **Revised:** 3 Jul 2026 **Accepted:** 27 Jul 2026 **Published:** 10 Aug 2026

Academic Editor: Hao Liu
Copy Editor: Ping Zhang
Production Editor: Ping Zhang

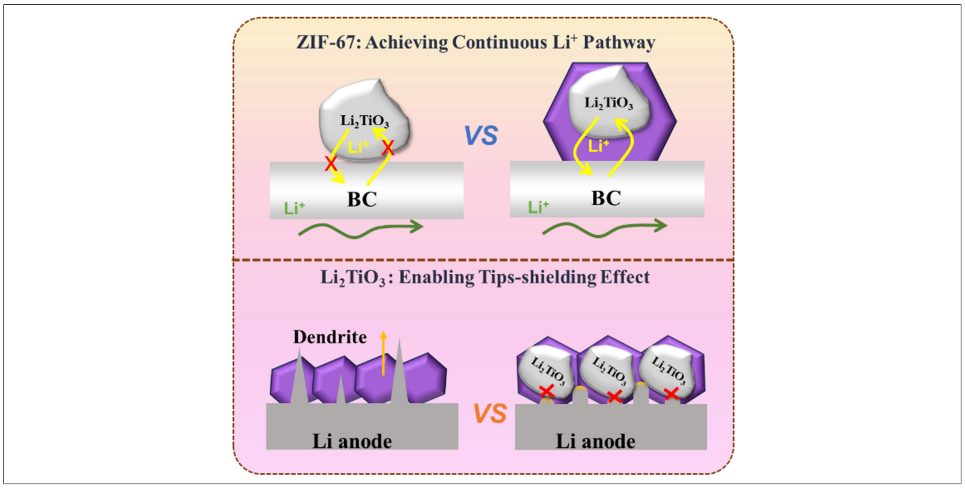

Abstract

Developing low-cost and renewable quasi-solid-state electrolytes (QSSEs) is critical for advancing energy storage technologies. Cellulose-based QSSEs have attracted considerable attention for their inherent renewability and cost advantages. However, discontinuous Li⁺ conduction pathways within cellulose frameworks severely limit their development as advanced electrolyte materials. Herein, an "ion-bridge" strategy is proposed, in which zeolitic imidazolate framework-67 (ZIF-67) serves as a bridge to connect α-Li_2TiO_3 and bacterial cellulose (BC), forming a BC/ZIF-67@Li_2TiO_3 hybrid electrolyte. This strategy effectively constructs interconnected long-range Li⁺ transport channels within the electrolyte, achieving a high ionic conductivity of 2.3×10^{-3} S cm^{-1} and a lithium-ion transference number of 0.81. Notably, α-Li_2TiO_3 serves as a highly favorable filler with excellent Li⁺ conductivity. Moreover, it provides an "active defense" mechanism

[1]Key Laboratory of Functional Materials Physics and Chemistry of the Ministry of Education, Jilin Normal University, Changchun 130103, Jilin, China.
[2]College of Chemistry, Jilin Normal University, Siping 136000, Jilin, China.
[3]Institute for Clean Energy Technology, North China Electric Power University, Beijing 102206, China.
[4]Beijing Synchrotron Radiation Facility, Institute of High Energy Physics, Chinese Academy of Sciences, Beijing 100049, China.
[5]Changbaishan Laboratory, Jilin University, Changchun 130012, Jilin, China.

***Correspondence to:** Prof. Ming Feng, Key Laboratory of Functional Materials Physics and Chemistry of the Ministry of Education, Jilin Normal University, Changchun 130103, Jilin, China. E-mail: mingfeng@jlnu.edu.cn; Dr. Rui Gao, Institute for Clean Energy Technology, North China Electric Power University, Beijing 102206, China. E-mail: r55gao@ncepu.edu.cn

against lithium dendrites through a tip-shielding effect, thereby reducing the risk of dendrite penetration. The Li|BC/ZIF-67@Li_2TiO_3|$LiFePO_4$ (LFP) full cell demonstrates exceptional cycling stability, retaining 89% of its initial capacity after 900 cycles at 1 C. This work provides a robust strategy for developing QSSEs that balance electrochemical performance and sustainability.

INTRODUCTION

The rapidly increasing demand for advanced energy storage systems has driven the development of next-generation chemical power sources with low cost and high energy density[1]. However, with the continuous increase in energy density and the expansion of application scenarios, safety concerns have become a critical bottleneck[2,3]. In particular, the flammability of conventional liquid electrolytes poses a major safety challenge. Batteries with solid-state electrolytes have emerged as a promising solution to these safety issues, while also offering the additional advantage of compatibility with lithium metal anodes for achieving higher energy densities[4-6]. Consequently, substantial research efforts have been devoted to exploring solid-state electrolytes with high ionic conductivity, a wide electrochemical window, and robust interfacial stability with lithium metal anodes[7,8].

Currently, solid-state electrolyte materials primarily include inorganic oxide electrolytes[9,10], sulfide electrolytes[11], and polymer electrolytes[12]. Although inorganic solid electrolytes exhibit impressive ionic conductivity and mechanical strength, they are often limited by poor interfacial contact stability arising from grain boundary space-charge layers[13], the air sensitivity of sulfide electrolytes[14], and the chemical instability of oxide electrolytes toward metallic lithium[15]. In contrast, polymer electrolytes provide better interfacial wettability but suffer from low room-temperature ionic conductivity and a narrow electrochemical window[16]. Therefore, conventional polymer electrolytes may not fully meet the requirements for the practical commercialization of solid-state batteries. To overcome these limitations, incorporating functional inorganic fillers into polymer matrices and synergistically combining them with a limited amount of liquid electrolyte has emerged as an effective strategy for constructing hybrid quasi-solid-state electrolytes (QSSEs). In these systems, the liquid electrolyte serves as a source of lithium salts, enabling simultaneous improvements in safety and electrochemical kinetics[17]. However, conventional hybrid QSSEs still face a trade-off between stability and ionic transport, primarily due to poor organic/inorganic interfacial compatibility and the absence of continuous ion-conduction pathways, which lead to high interfacial resistance and phase separation[18,19].

Cellulose-based electrolytes have attracted growing attention for their abundance, cost-effectiveness, exceptional chemical stability, and inherent flexibility[20]. In particular, the abundant oxygen-containing functional groups on the cellulose surface facilitate lithium salt dissolution, thereby improving ionic conductivity. Compared with petroleum-derived polymer-based electrolytes [e.g., Poly(ethylene oxide) (PEO) and Poly(methyl methacrylate) (PMMA)], cellulose exhibits enhanced interfacial affinity toward inorganic fillers. This advantage is attributed to its abundant polar functional groups and unique semi-crystalline fibrillar structure, which provide strong anchoring sites for fillers, effectively suppressing macroscopic phase separation and ensuring a more robust composite interface[21]. For example, Wang *et al.*[22] developed an ion-conductive molecular grafting strategy to fabricate cellulose acetate-based electrolytes (CLA-CN LATP), which exhibited superior electrochemical performance compared with PEO-based QSSEs. Similarly, Xu *et al.*[23] employed *in situ* polymerization of cyanoethyl cellulose to construct a coordination layer on garnet-type fillers, effectively stabilizing the organic-inorganic interface. However, direct chemical modification or specialized synthesis of cellulose frameworks to enhance electrochemical performance remains challenging. These approaches often require specific cellulose precursors, thereby increasing material costs and fabrication complexity. Therefore, there is an urgent need to develop more versatile and

cost-effective strategies compatible with a broader range of commercially available cellulose materials, enabling simplified fabrication processes without compromising electrochemical performance.

Studies have shown that introducing inorganic fillers into cellulose can disrupt cellulose crystallinity, thereby enhancing ionic conductivity. This approach is broadly applicable to both natural and synthetic cellulose sources. Nevertheless, owing to the limited functional groups on the surfaces of inorganic fillers, this method often fails to achieve strong interfacial bonding between organic and inorganic components[24,25]. Such inherent incompatibility can result in poor filler dispersion and compromised structural integrity of the composite electrolyte. Inspired by modification strategies for polymer electrolytes, the construction of ion-bridge channels at organic-inorganic interfaces has emerged as an effective approach to improving compatibility and preventing delamination. These channels can also facilitate rapid surface ion migration. For example, Mo *et al.*[26] achieved a bridging design by introducing siloxane segments, which enhanced lithium-ion transport and strengthened the interaction between the electrode and electrolyte. However, most existing bridging methods rely on chemical bonding, which typically exhibits a limited effective range and remains susceptible to environmental fluctuations. Recent studies have suggested that integrating cellulose with metal-organic frameworks (MOFs) featuring continuous spatial pores can further improve ionic conductivity. MOFs with polar functional groups and periodic porous structures can serve as efficient ion-bridge mediators to regulate interfacial Li^+ desolvation and migration behaviors, optimize ion-transport kinetics, and reduce interfacial resistance in hybrid electrolyte systems[27]. Zheng *et al.*[28] designed a "tree trunk" structured electrolyte by coating a cellulose-based framework with an *in situ* grown MOF layer to enhance conduction efficiency. Cheng *et al.*[29] employed Cu-MOF-loaded cellulose to alleviate concentration polarization and suppress dendrite growth. Despite these advances, MOFs in current systems often function merely as passive carriers, relying primarily on their intrinsic porosity for ion transport. This limitation frequently results in persistent issues, including interfacial impedance and insufficient integration during composite fabrication. Therefore, constructing a dedicated bridging layer using porous materials to actively connect organic and inorganic matrices may provide an effective strategy for improving bridging efficiency. Furthermore, developing materials capable of adaptively responding to fluctuations associated with lithium dendrite growth remains a critical yet unresolved challenge.

Herein, to address the persistent challenges of high interfacial resistance and discontinuous Li^+ conduction between organic and inorganic phases, a novel cellulose-based hybrid QSSE was developed, in which zeolitic imidazolate framework-67 (ZIF-67) serves as an ion bridge to crosslink the bacterial cellulose (BC) scaffold and α-Li_2TiO_3 particles. Specifically, cubic α-Li_2TiO_3 possesses a disordered cation distribution, which provides diverse and interconnected interstitial sites that substantially reduce the energy barrier for Li^+ hopping. This structural feature aligns well with the objective of constructing continuous Li^+ transport pathways, while BC serves as a supporting framework. Through the bridging effect of ZIF-67, the as-prepared BC/ZIF-67@Li_2TiO_3 QSSE enables long-range Li^+ transport channels, resulting in enhanced ionic conductivity and an increased Li^+ transference number (t_{Li^+}). Furthermore, this work reveals that α-Li_2TiO_3 not only functions as an ionic conductor but also provides active sites for suppressing dendrite growth through the "tip-shielding effect". This autonomous self-defense mechanism, combined with the optimized organic-inorganic interface, improves battery safety by mitigating the risks of thermal runaway and short circuits.

EXPERIMENTAL

Fabrication of QSSE

BC membranes were prepared by a simple filtration method. Briefly, 30 g of BC fiber suspension (containing 0.13 g of fibers) was dispersed in 300 mL of deionized distilled water (DDI water) and washed several times to remove residual additives. The BC suspension was purchased from Guilin Qihong Technology Co., Ltd.,

with fiber diameters of 50-100 nm and lengths of approximately 20 μm. All other reagents were purchased from Aladdin Reagent. The purified fibers were collected by centrifugation and dehydrated by washing with 150 mL of absolute ethanol four times. The resulting fibers were then redispersed in absolute ethanol to obtain a uniform suspension. ZIF-67 MOF and α-Li_2TiO_3 were prepared according to previously reported methods[30,31]. Briefly, 1.746 g of $Co(NO_3)_2 \cdot 6H_2O$ was dissolved in a mixed solvent containing 20 mL of methanol and 20 mL of ethanol to obtain a pink transparent solution (solution A). Subsequently, 1.97 g of 2-methylimidazole was dissolved in a mixed solvent containing 20 mL of methanol and 20 mL of ethanol under magnetic stirring to obtain a clear solution (solution B). Then, 0.3 g of α-Li_2TiO_3 was added to solution B. Solution A was subsequently added dropwise to solution B under continuous magnetic stirring. The resulting mixture was maintained at room temperature in a ventilated environment for 24 h. The precipitate was collected by centrifugation, washed three times with the corresponding solvent, and finally vacuum-dried at 60 °C for 12 h to obtain ZIF-67@Li_2TiO_3.

In a typical procedure, 0.1 g of ZIF-67 (or 0.1 g of ZIF-67@Li_2TiO_3) was dispersed in 25 mL of BC suspension and continuously stirred for 12 h to ensure homogeneous dispersion. Subsequently, 6 mL of the resulting mixture was subjected to vacuum filtration to fabricate the composite membranes, denoted as BC/ZIF-67 and BC/ZIF-67@Li_2TiO_3, respectively.

The final hybrid QSSEs were obtained through a lithiation process. Specifically, the as-prepared membranes were immersed in a $LiPF_6$/EC/DMC electrolyte for 2 h. After pre-drying at room temperature for 24 h, the membranes were further vacuum-dried at 80 °C to completely remove residual organic solvents, while retaining the lithium salt within the framework. All lithiation processes were conducted in an Ar-filled glovebox with H_2O and O_2 concentrations below 0.1 ppm.

Structure characterization

The crystal structures of the powder samples and composite membranes were analyzed by X-ray powder diffraction (XRD, PANalytical) over a 2θ range of 5°-90°. The morphologies of the samples were characterized using an S-5500 ultra-high-resolution scanning electron microscope (SEM) (Hitachi) and a Talos F200X G2 field-emission transmission electron microscope (Thermo Fisher Scientific). The functional groups of the samples were analyzed by Fourier transform infrared spectroscopy (FTIR) using an iS50 spectrometer (Thermo Fisher Scientific). X-ray absorption spectra of the samples were collected at the Beijing Synchrotron Radiation Facility (BSRF). The wettability of the electrolyte membranes was evaluated using a contact angle instrument (Theta A20, Biolin Scientific, Finland). Electrochemical performance tests were conducted using an electrochemical workstation (1470E, Solartron, UK). Constant-voltage and constant-current charge-discharge tests were performed using a high-performance battery testing system (CT-ZWJ-4'S-010, Shenzhen Xinwei New Energy Technology Co., Ltd., China). The thermal properties of the samples were investigated using a simultaneous thermal analyzer (STA449F5, Netzsch, Germany).

Model implementation

This mechano-electrochemical model was simulated using the finite element method in COMSOL Multiphysics 6.3. To simplify the model, an electrolyte region with dimensions of 100 μm × 100 μm was constructed for the simulation. An initial dendrite morphology was established within this region, consisting of a trapezoid-like dendrite with a top width of 5 μm, a bottom width of 15 μm, and a height of 50 μm. The two sharp corners were rounded using a fillet. The distance between adjacent dendrites was set to 40 μm. The entire top boundary was defined as the Li growth boundary. The simulation considered two types of electrolyte materials: BC and BC/ZIF-67@Li_2TiO_3 QSSE. The BC/ZIF-67@Li_2TiO_3 QSSE exhibited a tip-shielding effect that suppressed the vertical growth of lithium dendrites. To ensure a reliable comparison, the initial lithium dendrite dimensions in both models were set to be identical.

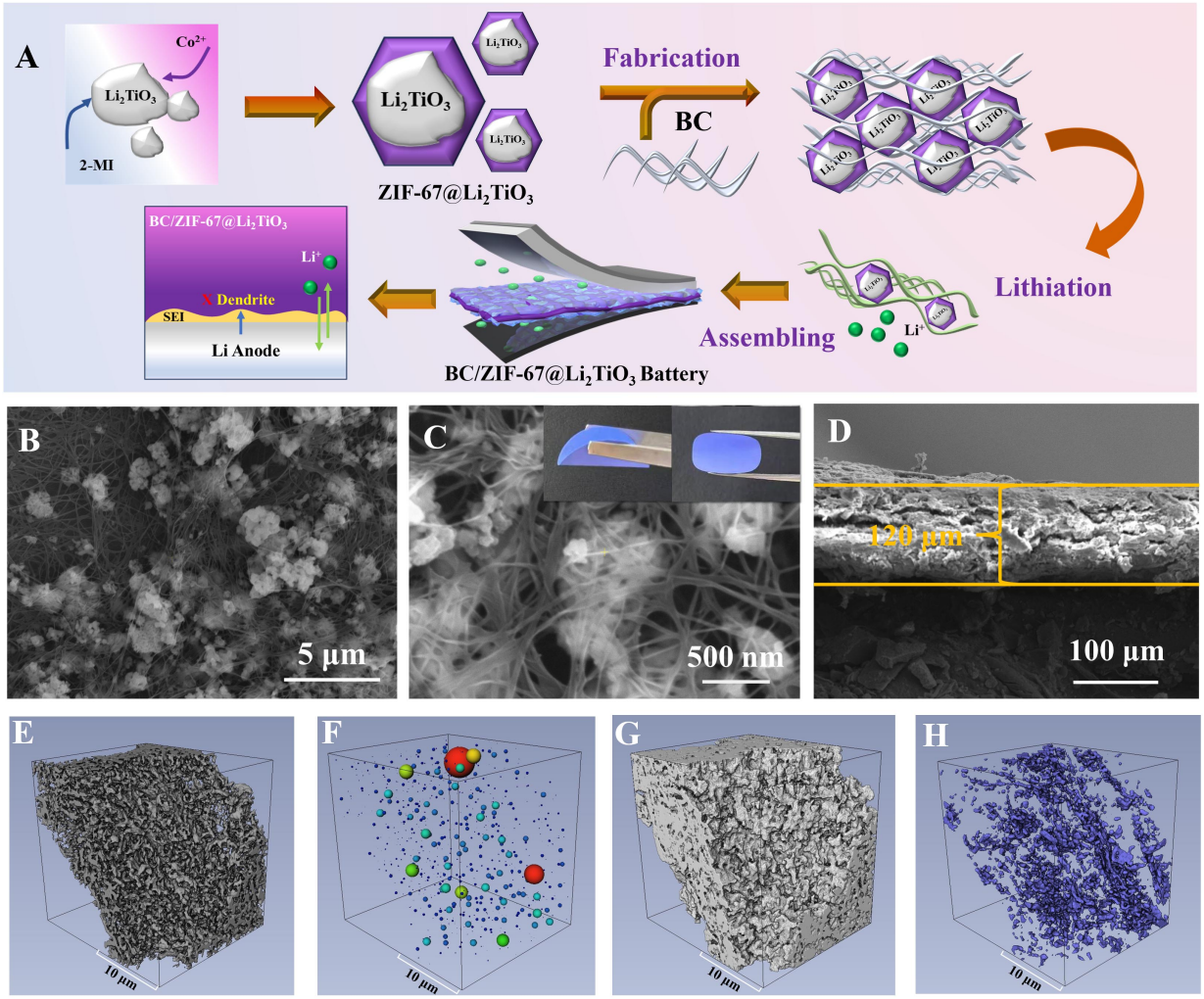

Figure 1. Synthesis schematic diagram and microscopic characterization. (A) Schematic diagram of BC/ZIF-67@Li_2TiO_3 QSSE preparation and mechanism of action; (B and C) The SEM images of the BC/ZIF-67@Li_2TiO_3 membrane, top view at different magnifications. The insert image of (C) shows the flexibility of the membrane; (D) Cross-sectional view; (E and F) Nano-CT of BC/ZIF-67@Li_2TiO_3 QSSE electrolyte spatial distribution of void structures and spherical model aperture distribution; (G) The spatial structure of BC/ZIF-67@Li_2TiO_3; (H) Spatial distribution of ZIF-67@Li_2TiO_3. BC: Bacterial cellulose; ZIF-67: zeolitic imidazolate framework-67; QSSEs: quasi-solid-state electrolytes; SEM: scanning electron microscope.

The simulation consisted of a transient step. A potential of 0 V was applied to the surfaces of all negative electrodes, while a potential of 0.1 V was applied to the positive electrode surfaces. The initial Li^+ ion concentration in the electrolyte was set to 1,000 mol m^{-3}, and the Li plating time was set to 50 s.

RESULTS AND DISCUSSION

Structure features of BC/ZIF-67@Li_2TiO_3

Figure 1A illustrates the design strategy and synthetic route of the BC/ZIF-67@Li_2TiO_3 hybrid QSSE. To achieve rapid Li^+ bridging, ZIF-67 was first deposited onto the surface of α-Li_2TiO_3 through an *in situ* growth process. Here, low-temperature α-Li_2TiO_3 was selected because it provides diverse and interconnected interstitial sites, which substantially reduce the energy barrier for Li^+ hopping[32]. Subsequently, the as-prepared ZIF-67@Li_2TiO_3 powder was incorporated into a BC suspension. Owing to the strong interaction between BC and the Co sites of ZIF-67, the ZIF-67@Li_2TiO_3 hybrid was uniformly anchored onto the BC framework. This three-dimensional cross-linked network structure provides a solid foundation for the excellent flexibility and intimate interfacial contact of the electrolyte. The BC/ZIF-67@Li_2TiO_3 hybrid membrane obtained by vacuum filtration exhibited good flexibility and a characteristic purple color. The final activation of the QSSE was achieved through a lithiation process.

Specifically, this innovative electrolyte architecture was designed with a BC matrix that provides a unique three-dimensional interconnected porous network. This structure not only facilitates Li^+ migration but also enables intimate interfacial contact with electrodes owing to the inherent mechanical flexibility of BC. As a representative MOF material, ZIF-67 features a high specific surface area and a tunable pore structure. When integrated with BC, ZIF-67 performs dual functions: first, its well-defined microporous channels regulate Li^+ transport kinetics and effectively mitigate concentration polarization[33]; second, ZIF-67 acts as a "Li^+ bridge" that chemically and physically couples organic cellulose fibers with inorganic fillers, thereby establishing continuous and highly ordered ion-conduction pathways. Importantly, the incorporation of α-Li_2TiO_3 further elevates the electrolyte from a passive physical barrier to an active defense system.

To elucidate the structural characteristics of the as-synthesized QSSEs, multi-scale imaging techniques were employed to investigate the morphological features and spatial architecture of the BC/ZIF-67@Li_2TiO_3 hybrid in detail. The surface morphologies of the raw materials and composite membranes were characterized by SEM. Supplementary Figure 1A-C presents the SEM images of bare ZIF-67 and ZIF-67@Li_2TiO_3. Compared with bare ZIF-67, ZIF-67@Li_2TiO_3 exhibits an irregular morphology with pronounced particle aggregation. This behavior is primarily attributed to the *in situ* growth of ZIF-67 on the surface of Li_2TiO_3, where ZIF-67 acts as a molecular binder that integrates individual nanoparticles into larger aggregates. Supplementary Figure 1C further reveals the detailed structure and elemental distribution of ZIF-67@Li_2TiO_3. The energy-dispersive X-ray spectroscopy (EDS) mapping results [Supplementary Figure 1D-F] clearly confirm the presence of ZIF-67 on the surface of Li_2TiO_3. According to space-charge layer theory[1], excessive Li_2TiO_3/Li_2TiO_3 grain boundaries can deplete the local Li^+ concentration at these interfaces, thereby hindering Li^+ conduction. The introduced ZIF-67-layer acts as an *in situ* molecular bridge that encapsulates Li_2TiO_3 particles, effectively preventing direct Li_2TiO_3/Li_2TiO_3 grain-boundary contact and reducing the number of grain boundaries associated with interfacial resistance. Calculations of powder ionic conductivity indicate that the introduction of ZIF-67 increases the ionic conductivity from 2.86×10^{-7} S cm^{-1} to 9.87×10^{-7} S cm^{-1}. As shown in Supplementary Figure 2, the mass ratio of ZIF-67 to α-Li_2TiO_3 and the total filler content within the BC matrix were systematically optimized through morphological and electrochemical characterizations. A loading amount of 0.3 g α-Li_2TiO_3 was determined to be optimal, enabling uniform filler dispersion, continuous ion-transport networks, and superior overall performance.

Figure 1B, C and Supplementary Figure 3A, B show images of the assembled membranes. In Figure 1B and C, BC fibers are clearly observed to wrap around the ZIF-67@Li_2TiO_3 particles. The inset images in Figure 1C demonstrate that the BC/ZIF-67@Li_2TiO_3 membrane exhibits excellent flexibility. The cross-sectional SEM image of the BC/ZIF-67@Li_2TiO_3 membrane reveals a highly dense and integrated structure with a uniform thickness of approximately 120 μm, as shown in Figure 1D. EDS mapping in Supplementary Figure 4 indicates that Ti, Co, C, O, and N are uniformly distributed throughout the membrane, consistent with the structural design of the composite electrolyte. The homogeneous distribution of active components is essential for constructing continuous Li^+ transport pathways and maintaining stable ionic flux across the electrolyte.

To further characterize the spatial continuity of the electrolyte, nano-resolution X-ray computed tomography (nano-CT) was employed for high-resolution three-dimensional structural analysis. Figure 1E presents the reconstructed three-dimensional volume distribution of internal pores. The uniform pore distribution facilitates efficient infiltration and retention of the liquid electrolyte, resulting in a more homogeneous Li^+ distribution during lithiation. Figure 1F presents the simulated pore size distribution, in which the dimensions and color gradients of the spheres represent local pore diameters, revealing a remarkably uniform pore size throughout the scanned volume. This structural homogeneity is primarily attributed to the continuous and interconnected three-dimensional network formed by cellulose nanofibers.

Furthermore, the volume distribution of the QSSE was reconstructed based on the nano-CT results, as shown in Figure 1G. Figure 1H was extracted from Figure 1G and illustrates the distribution of ZIF-67@Li_2TiO_3. Supplementary Figure 5 presents an overlay of BC and Li_2TiO_3 distributions. It can be observed that ZIF-67@Li_2TiO_3 is encapsulated within the cellulose matrix, which is highly consistent with the SEM observations and closely matches the original structural design. This structural feature enables ZIF-67 to function as an ionic bridge connecting the BC matrix and Li_2TiO_3 fillers, thereby providing a robust structural foundation for enhancing electrolyte performance. Multi-scale morphological characterization further confirms that the as-prepared membrane possesses a well-defined architecture consistent with the proposed design.

Furthermore, X-ray diffraction (XRD) measurements were performed to verify the formation of each crystalline phase. As shown in Supplementary Figure 6A, the XRD pattern of Li_2TiO_3 exhibits characteristic diffraction peaks at 43° and 64°, corresponding to cubic α-Li_2TiO_3[31]. Herein, α-Li_2TiO_3 was strategically selected as the inorganic filler owing to its superior intrinsic ionic conductivity. Compared with other Li_2TiO_3 phases, α-Li_2TiO_3 possesses a disordered cation distribution, which provides diverse and interconnected interstitial sites and substantially reduces the energy barrier for Li^+ hopping. For the XRD pattern of BC/ZIF-67@Li_2TiO_3, all characteristic diffraction peaks originating from BC, α-Li_2TiO_3, and ZIF-67 can be well indexed [Supplementary Figure 6B]. The diffraction peaks at 2θ = 7.3°, 14.9°, and 22.3° are assigned to the (001), (112), and (222) planes of ZIF-67, respectively[34]. In addition, the two characteristic peaks at 14.3° and 22.5° correspond to the (110) and (200) planes of BC[35]. The diffraction peaks at 43° and 64° are attributed to α-Li_2TiO_3, confirming its successful integration with ZIF-67 and BC.

To investigate the surface structure and interfacial compatibility, molecular spectroscopy and X-ray absorption spectroscopy analyses were conducted. FTIR measurements of the prepared membranes were performed [Figure 2A-C] to analyze their functional groups and chemical compositions. In Figure 2A and B, the absorption band at 1,580 cm^{-1} is assigned to the stretching vibration of the C=N bond in ZIF-67. The broad absorption peaks at 3,348 cm^{-1}, 2,898 cm^{-1}, and 1,058 cm^{-1} correspond to the O-H stretching, C-H asymmetric stretching, and C-O-C vibrations of BC, respectively [Figure 2A]. These abundant functional groups provide favorable sites for Li^+ migration along the BC surface[36]. The peaks at 1,141 cm^{-1} and 755 cm^{-1} are attributed to the in-plane vibration of the imidazole ring in ZIF-67. After integration with BC, the decreased absorption intensity in the range of 630-750 cm^{-1} indicates that the vibrations outside the imidazole ring are affected by cellulose, confirming the interaction between BC and ZIF-67. The inset of Figure 2B reveals a distinct intensity variation in the O-H stretching region, suggesting a strong chemical interaction between ZIF-67 and Li_2TiO_3 during the formation of ZIF-67@Li_2TiO_3. In Figure 2C, notably, the Co-N stretching mode of BC/ZIF-67 exhibits a blue shift from 423 cm^{-1} to 424 cm^{-1} after the BC crosslinking reaction, indicating that the Co sites in ZIF-67 successfully interact with cellulose molecular chains. Furthermore, Supplementary Figure 7 shows that the band at 1,567 cm^{-1} in the ZIF-67 spectrum corresponds to the stretching and bending vibrations of the C=N bond in the imidazole ring. This peak is slightly shifted to 1,580 cm^{-1} in the BC/ZIF-67@Li_2TiO_3 spectrum, further demonstrating that BC can effectively combine with ZIF-67@Li_2TiO_3 through the bridging effect of ZIF-67[30]. Moreover, owing to the strong characteristic absorption of α-Li_2TiO_3 below 1,000 cm^{-1}, a pronounced baseline depression is observed for the BC/ZIF-67@Li_2TiO_3 composite in the range of 450-1,000 cm^{-1}. Therefore, the FTIR analysis provides compelling evidence for robust molecular-level coupling between α-Li_2TiO_3 and the BC matrix. This intimate interfacial bonding is essential for enabling ZIF-67 to function as an efficient "ionic bridge", facilitating seamless Li^+ conduction across the multi-component electrolyte.

The surface elemental compositions and chemical valence states of the BC/ZIF-67 and BC/ZIF-67@Li_2TiO_3 membranes were investigated using X-ray photoelectron spectroscopy (XPS) [Figure 2D-F] and Supplementary Figures 8 and 9. The high-resolution C 1s spectrum of the BC/ZIF-67@Li_2TiO_3 hybrid

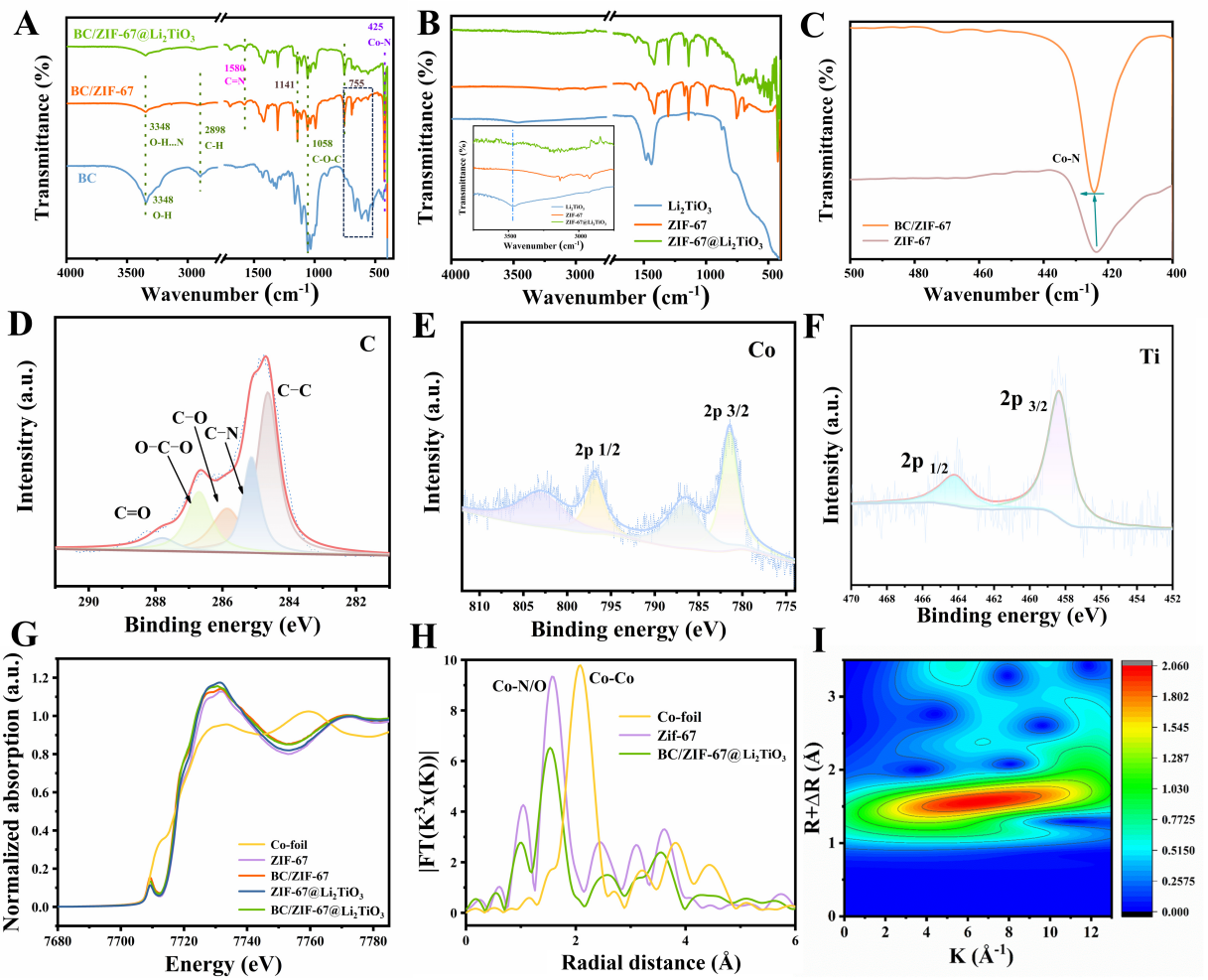

Figure 2. (A) FTIR analysis of BC, BC/ZIF-67, and BC/ZIF-67@Li_2TiO_3 membranes; (B) FTIR analysis of α-Li_2TiO_3, ZIF-67, and ZIF-67@Li_2TiO_3 powder; (C) FTIR analysis of BC/ZIF-67 membrane and ZIF-67 powder; The XPS spectra of (D) C, (E) Co, and (F) Ti in the BC/ZIF-67@Li_2TiO_3 membrane; (G) XANES for the Co-K edge of Co-foil, ZIF-67, BC/ZIF-67, ZIF-67@Li_2TiO_3, and the BC/ZIF-67@Li_2TiO_3 membrane; (H) The Fourier transform EXAFS for the Co K edge of Co foil, ZIF-67, and the BC/ZIF-67@Li_2TiO_3 membrane; (I) Wavelet transition of the BC/ZIF-67@Li_2TiO_3 membrane for the k^3-weighted EXAFS signals. BC: Bacterial cellulose; ZIF-67: zeolitic imidazolate framework-67; QSSEs: quasi-solid-state electrolytes; XANES: X-ray absorption near-edge structure; FTIR: fourier transform infrared spectroscopy; XPS: X-ray photoelectron spectroscopy; EXAFS: extended X-ray absorption fine structure.

[Figure 2D] can be deconvoluted into five distinct carbon chemical environments. The peaks at 284.81 eV and 285.48 eV are assigned to C-C and C-N bonds (derived from 2-methylimidazole ligands), respectively. Characteristic peaks associated with the BC matrix are observed at 286.1 eV (C-O) and 287.3 eV (O-C-O). Notably, a prominent signal at 287.79 eV corresponding to C=O bonds is identified, which is partially attributed to the chemical interaction between the hydroxyl groups of BCs and the imidazole ligands. In Supplementary Figure 8, the N 1s spectrum exhibits a peak at 398.84 eV, corresponding to Co-N bonds in pyridinic nitrogen environments[37]. As shown in Figure 2E, the Co 2p spectrum displays two main peaks at 781.49 eV (Co $2p_{3}/_{2}$) and 796.99 eV (Co $2p_{1}/_{2}$)[38], accompanied by satellite peaks at 786.37 eV and 802.47 eV. The high-resolution Ti 2p XPS spectrum is presented in Figure 2F. The obtained spectrum is consistent with that of α-Li_2TiO_3, confirming that Ti in α-Li_2TiO_3 exists in the +4 oxidation state[39]. Supplementary Figure 9A-C presents the XPS spectra of Co, N, and O elements in the BC/ZIF-67 membrane. The O 1s peak can be fitted into three components with binding energies of 530.7, 532.74, and 534.32 eV, which are assigned to

O-H (BC), O-C (BC), and O-Co (derived from BC/ZIF-67) bonds, respectively. The fitted O 1s spectrum enables the specific binding energy of the Co-O bond to be resolved, providing direct evidence of the chemical interaction between ZIF-67 and BC. These combined results confirm the successful integration of BC and ZIF-67[32]. X-ray absorption fine structure (XAFS) analysis was further conducted to investigate the local coordination environment of Co species [Figure 2G]. The unchanged absorption edge position (E_0) indicates that the valence state of Co species remains stable. The BC/ZIF-67@Li_2TiO_3 sample exhibits a distinct pre-edge peak, demonstrating that the central Co atoms maintain a stable tetrahedral coordination geometry. Specifically, this pre-edge feature originates from electronic excitation into the 3d orbitals, which is more readily observed when the metal center adopts this specific four-coordinated spatial configuration[40]. Compared with pristine ZIF-67, the pre-edge intensity of BC/ZIF-67@Li_2TiO_3 decreases, indicating a modification of the Co coordination environment[41]. This result further supports our previous conclusion that Co sites enhance the integration between ZIF-67 and BC through coordination with surface functional groups. Figure 2H presents the R-space results of the extended X-ray absorption fine structure (EXAFS) of these samples. The peak at approximately 1.5 Å in the Co EXAFS spectrum is attributed to Co-N coordination[42]. The wavelet transforms (WT) analysis of the k^3-weighted EXAFS signal for the BC/ZIF-67@Li_2TiO_3 membrane is shown in Figure 2I. The contour plot of the BC/ZIF-67@Li_2TiO_3 membrane exhibits maximum intensity at approximately 1.5 Å, corresponding to the Co-N contribution. Compared with pristine ZIF-67, the coordination shell of the hybrid exhibits a slight shift toward lower R values with a substantial decrease in intensity, which may be attributed to the strong chemical interaction between the BC matrix and Co active sites. These results collectively demonstrate the successful construction of the designed hybrid structure. The prepared electrolyte was subsequently employed for battery assembly to evaluate its electrochemical performance.

Electrochemical performance of BC/ZIF-67@Li_2TiO_3

To evaluate the wettability of the membranes, the contact angles of the three samples were measured. The results are presented in Figure 3A and Supplementary Figure 10. The contact angle of the BC membrane was 23.43° after 1 s of immersion, whereas that of the BC/ZIF-67 membrane decreased to 4° after 1 s. In contrast, the liquid electrolyte was completely absorbed into the BC/ZIF-67@Li_2TiO_3 membrane within 1 s. These results demonstrate that the BC/ZIF-67@Li_2TiO_3 membrane exhibits superior electrolyte wettability compared with the other membranes, which can facilitate rapid electrolyte penetration and promote subsequent lithiation for the preparation of QSSEs[30,43]. The as-prepared BC/ZIF-67@Li_2TiO_3 membrane underwent a controlled lithiation process to activate its internal ion-conduction network. According to the thermogravimetric analysis (TGA) curve in Supplementary Figure 11, only approximately 1% of the liquid phase remains in the lithiated electrolyte. Therefore, the ionic conductivity mechanism investigated in this work is primarily governed by Li^+ migration through the solid phase. Subsequently, the lithiated electrolyte was assembled into lithium metal batteries to evaluate its comprehensive electrochemical performance. Before each electrochemical measurement, the assembled batteries were allowed to rest at room temperature for 4 h for activation.

To measure the ionic conductivity (σ), QSSEs based on four different membranes, namely BC, BC/ZIF-67, BC/Li_2TiO_3, and BC/ZIF-67@Li_2TiO_3, were prepared and assembled into lithium metal batteries. Figure 3B and Supplementary Figures 12-14 compare the t_{Li+} and ionic conductivity values of these samples. Among all samples, BC/Li_2TiO_3 exhibits the lowest t_{Li+} (0.22) and ionic conductivity (1.0×10^{-4} S cm^{-1}), which is attributed to the poor interfacial compatibility between BC and inorganic Li_2TiO_3. As shown in Figure 3B, both BC/ZIF-67 and BC/ZIF-67@Li_2TiO_3 exhibit an identical t_{Li+} value of 0.81. This similarity is mainly attributed to ZIF-67's ability to immobilize free anions while bridging the BC matrix, thereby increasing t_{Li+}. Although both samples possess the same t_{Li+} value, the ionic conductivity of BC/ZIF-67@Li_2TiO_3 (2.3×10^{-3} S cm^{-1}) is higher than that of BC/ZIF-67 (1.1×10^{-4} S cm^{-1}). This difference indicates that the local carrier

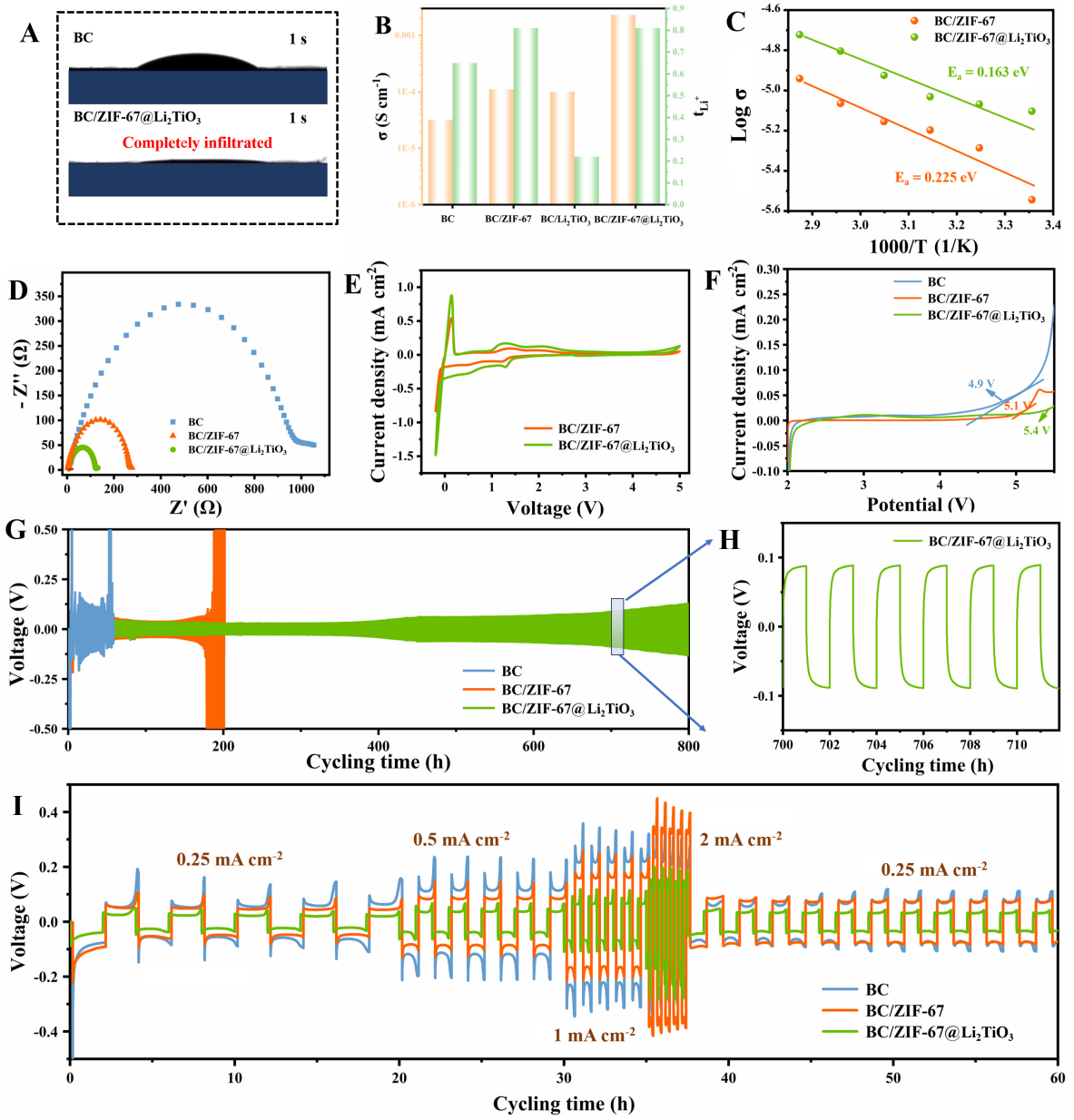

Figure 3. Li^+ transport properties and electrochemical performances of QSSE. (A) Precursor solution contact angle of membranes at 1 s; (B) The ionic conductivity and Li^+ transference number of different QSSEs at room temperature; (C) Arrhenius plots of ionic conductivity of BC/ZIF-67 and BC/ZIF-67@Li_2TiO_3 QSSEs; (D) EIS of Li||Li symmetric cells at pristine state; (E) CV curves of Li||SS cells with a sweep rate of 5 mV/s; (F) LSV curves of different QSSEs; (G and H) Long-term cycling performance of Li||Li symmetrical batteries under a current density of 0.5 mA cm^{-2}; (I) Potential-time curves of the symmetrical Li||Li cells with different QSSEs under current densities of 0.25, 0.5, 1, 2, and 0.25 mA cm^{-2}. BC: Bacterial cellulose; ZIF-67: zeolitic imidazolate framework-67; QSSEs: quasi-solid-state electrolytes; CV: cyclic voltammetry; LSV: linear sweep voltammetry.

concentration and ion-transport pathways at the BC/ZIF-67 interface are insufficient to establish efficient long-range Li^+ conduction. In contrast, within the BC/ZIF-67@Li_2TiO_3 system, the bridging effect of ZIF-67 combined with the highly conductive Li_2TiO_3 filler improves interfacial contact and reduces grain-boundary resistance. These results further confirm that ZIF-67 effectively constructs continuous and interconnected Li^+ transport pathways, as schematically illustrated in Figure 1A, thereby substantially enhancing the overall ionic conductivity.

Pure α-Li_2TiO_3 nanoparticles tend to undergo loose aggregation, resulting in poor interfacial contact and high interparticle resistance, which severely hinders Li^+ migration. After decoration with ZIF-67, the ZIF-67-layer acts as an ion-conductive bridge to alleviate particle aggregation, improve interfacial compatibility, and reduce interfacial impedance, thereby constructing continuous Li^+ transport pathways. Therefore, in the present study, only QSSEs based on BC, BC/ZIF-67, and BC/ZIF-67@Li_2TiO_3 were selected for further electrochemical evaluation.

Figure 3C presents the activation energy (E_a) calculated from Electrochemical impedance spectroscopy (EIS) measurements at different temperatures, with the corresponding impedance spectra shown in Supplementary Figure 15A and B. The Ea values of BC/ZIF-67 and BC/ZIF-67@Li_2TiO_3 are 0.225 eV and 0.163 eV, respectively. Notably, the BC/ZIF-67@Li_2TiO_3 electrolyte exhibits a lower Ea than BC/ZIF-67. This reduction can be attributed to the discrete BC network being bridged by ZIF-67@Li_2TiO_3 into a continuous and interconnected framework, providing efficient pathways for Li^+ transport. Owing to the strong interactions between ZIF-67 and both BC and Li_2TiO_3, the increased BC/ZIF and ZIF/Li_2TiO_3 interfacial regions facilitate Li^+ accumulation and promote the formation of continuous low-barrier ion-transport pathways[44]. Consequently, the Ea of the BC/ZIF-67@Li_2TiO_3 electrolyte is reduced.

Figure 3D shows the EIS results of Li||Li symmetric cells employing bare BC, BC/ZIF-67, and BC/ZIF-67@Li_2TiO_3 electrolytes. All EIS data were obtained using standard 2025 coin cells. The results demonstrate that the bare BC electrolyte exhibits a high resistance of 950 Ω. In contrast, the BC/ZIF-67@Li_2TiO_3 electrolyte exhibits lower interfacial and charge-transfer resistances than both bare BC and BC/ZIF-67 electrolytes. This substantial reduction in resistance provides strong evidence for the superior interfacial compatibility between the BC/ZIF-67@Li_2TiO_3 electrolyte and the lithium anode. Figure 3E presents the CV curves of the different electrolytes. Two predominant redox peaks appear near 0 V. Compared with BC/ZIF-67 (0.56 mA cm^{-2}), BC/ZIF-67@Li_2TiO_3 exhibits a higher peak current density, with a stripping peak current density of 0.88 mA cm^{-2}. As shown in the Linear sweep voltammetry (LSV) curves in Figure 3F, the electrochemical stability window (ESW) of the BC/ZIF-67@Li_2TiO_3 electrolyte reaches 5.4 V, which is wider than those of pure BC (4.9 V) and BC/ZIF-67 (5.1 V). This expanded electrochemical window improves compatibility with high-voltage cathode materials, demonstrating the great potential of the electrolyte for high-energy-density battery applications.

To evaluate the electrochemical stability of the BC/ZIF-67@Li_2TiO_3 electrolyte toward lithium metal anodes, three types of lithium symmetric cells were selected. Li|BC|Li, Li|BC/ZIF-67|Li, and Li|BC/ZIF-67@Li_2TiO_3|Li cells were assembled for long-term cycling tests at 0.5 mA cm^{-2} and rate performance tests under various current densities ranging from 0.25 mA cm^{-2} to 2 mA cm^{-2}, with a fixed capacity of 0.5 mAh cm^{-2}. As shown in Figure 3G, the Li|BC|Li cell exhibits a large voltage polarization of approximately 100 mV, accompanied by a steep voltage plateau. After cycling for 60 h, the voltage increases sharply, indicating accelerated degradation of the lithium plating/stripping process. The Li|BC/ZIF-67|Li cell exhibits a lower average polarization voltage of 56 mV, although a rapid voltage increase occurs after 180 h. This result suggests that the introduction of ZIF-67 enhances ion-transfer kinetics and reduces the lithium nucleation overpotential. With the incorporation of α-Li_2TiO_3, the cycle life of the symmetric cell is extended to 800 h, with an average polarization voltage of only 42 mV. The enlarged voltage profile in Figure 3H corresponds to a representative region at approximately 700 h during the long-term cycling test. Even after 700 h of continuous operation, the cell maintains a stable voltage profile without short-circuit failure, exhibiting only a slight increase in overpotential. These results demonstrate that the BC/ZIF-67@Li_2TiO_3 electrolyte enables highly reversible lithium plating/stripping over prolonged cycling. As shown in Figure 3I, rate performance tests were further conducted using Li symmetric cells. The polarization voltages of the BC/ZIF-67@Li_2TiO_3 electrolyte at current densities of 0.25, 0.5, 1.0, 2.0, and 0.25 mA cm^{-2} are 20, 35, 85, 95, and 20 mV, respectively. Notably,

after rate cycling, the polarization voltage reversibly returns to 20 mV at 0.25 mA cm^{-2}, demonstrating excellent structural stability. The Li|BC|Li cell exhibits the highest overpotential at each current density, mainly attributed to the limited short-range Li^+ transport pathways that hinder efficient ion migration. After modification with ZIF-67, the overpotential is reduced. Notably, the introduction of ZIF-67@Li_2TiO_3 results in the lowest charge-discharge polarization. These results confirm that ZIF-67 effectively facilitates Li^+ transport between individual cellulose fibers, thereby improving ion-conduction kinetics. Furthermore, the incorporation of Li_2TiO_3 as a highly ionic-conductive filler enables rapid ion transport, accelerating Li^+ transfer throughout the BC/ZIF-67@Li_2TiO_3 matrix.

The electrochemical results demonstrate the effectiveness of BC/ZIF-67@Li_2TiO_3 in improving overall electrochemical performance. Based on the material design and structural characterization, the enhanced performance can be primarily attributed to the bridging effect of ZIF-67. By tightly connecting BC fibers with Li_2TiO_3 fillers, ZIF-67 establishes continuous Li^+ transport pathways throughout the electrolyte matrix. This rapid ion-conduction capability, on the one hand, regulates Li^+ distribution at the anode interface, thereby suppressing dendrite formation and ensuring long-term cycling stability. On the other hand, it reduces the energy barrier for Li^+ migration, effectively mitigating polarization during lithium plating/stripping, particularly under high-rate conditions.

Mechanism and microscopic feature analysis

To further investigate the mechanism by which BC/ZIF-67@Li_2TiO_3 protects the lithium anode, the morphology of cycled anodes was characterized after long-term cycling. As shown in Figure 4A, the pristine Li anode exhibits a smooth and flat surface morphology. After cycling, almost no dead lithium or by-products are observed on the anode of the Li|BC/ZIF-67@Li_2TiO_3|Cu battery. The cycled anode maintains a morphology comparable to that of pristine lithium metal [Figure 4B]. This favorable behavior is attributed to the rationally designed QSSE structure, which facilitates the establishment of continuous Li^+ transport pathways. Moreover, the incorporation of α-Li_2TiO_3 enhances the regulation of electric field distribution at the lithium surface, thereby suppressing dendrite formation. In contrast, after cycling, the anode surface of the Li|BC/ZIF-67|Cu battery exhibits a higher accumulation of dead lithium and decomposition by-products, as shown in Figure 4C. Owing to its inferior ionic conductivity and limited short-range Li^+ transport pathways, the Li|BC|Cu battery exhibits the most severe anode degradation among the three systems, as shown in Figure 4D.

The structure and composition of the solid electrolyte interphase (SEI) formed on the anode were further investigated using Transmission electron microscopy (TEM) and corresponding EDS mapping. Figure 4E displays the morphology of the accumulated SEI layer deposited on the Cu substrate. Figure 4F and G present High-resolution transmission electron microscopy (HR-TEM) images of the SEI layer at different magnifications. As shown in Figure 4G, the observed lattice fringes of 3.87 Å and 2.32 Å can be assigned to lithium nitride (001) and lithium fluoride (111) nanocrystals, respectively. This result indicates that the SEI layer formed on the anode is primarily composed of inorganic compounds. Figure 4H presents the High-angle annular dark-field scanning transmission electron microscopy (HAADF-STEM) image and EDS mapping of the deposited SEI generated using the BC/ZIF-67@Li_2TiO_3 electrolyte. As revealed by the elemental mapping, the uniform distribution of F throughout the SEI layer further confirms the dominant presence of fluorinated species. According to previous reports[43], F- and N-enriched inorganic components within the SEI can effectively stabilize the anode/electrolyte interface and extend the cycling lifetime of lithium metal anodes. LiF is mainly derived from the decomposition of lithium hexafluorophosphate during the initial electrochemical processes. XPS analysis further confirms the enrichment of F- and N-containing species within the SEI layer. The F 1s spectrum exhibits a distinct peak at approximately 684.8 eV [Supplementary Figure 16A], which is attributed to LiF. Combined with the EDS mapping results, these

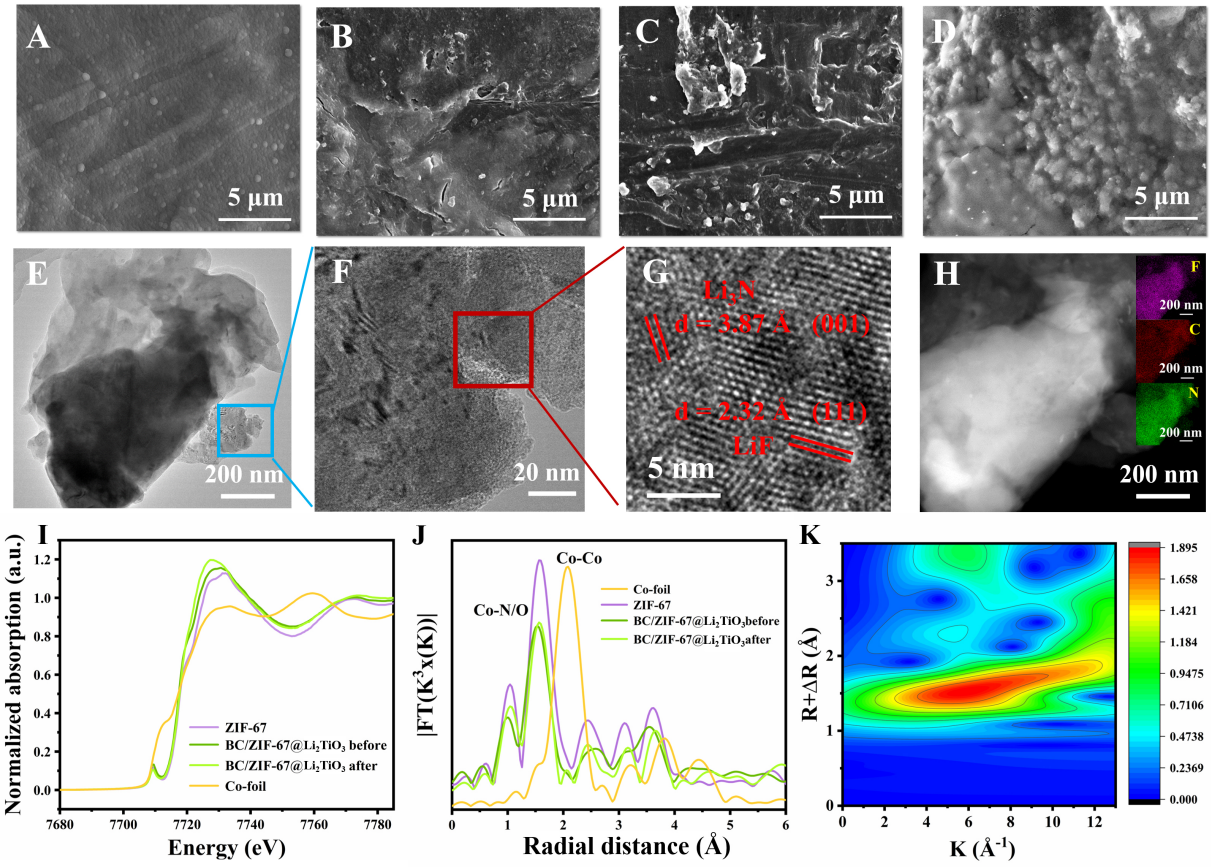

Figure 4. (A) SEM image of Li metal anode before cycling; (B) SEM image of Li metal anode after Li|BC/ZIF-67@Li_2TiO_3|Cu battery cycle; (C) SEM image of Li metal anode after Li|BC/ZIF-67|Cu battery cycle; (D) SEM image of Li metal anode after Li|BC|Cu battery cycle; (E) TEM image of the deposited Li metal anode after cycling in a Li|BC/ZIF-67@Li_2TiO_3|Cu cell; (F) Localized magnified image of the selected area in (E); (G) HRTEM of the selected region in (F); (H) HAADF-STEM image of the Li metal anode after cycling in a Li|BC/ZIF-67@Li_2TiO_3|Cu cell; the insert is energy-dispersive spectroscopic (EDS) maps of F, C, and N; (I) XANES and (J) the Fourier transform EXAFS for Co-K edge of Co-foil, ZIF-67 powder, and BC/ZIF-67@Li_2TiO_3 electrolyte before and after cycling; (K) Wavelet transform of the Co K-edge EXAFS signals for the BC/ZIF-67@Li_2TiO_3 electrolyte. BC: Bacterial cellulose; ZIF-67: zeolitic imidazolate framework-67; XANES: X-ray absorption near-edge structure; SEM: scanning electron microscope; TEM: transmission electron microscopy; HRTEM: high-resolution transmission electron microscopy; HAADF-STEM: high-angle annular dark-field scanning transmission electron microscopy; EXAFS: extended X-ray absorption fine structure.

findings indicate that BC/ZIF-67@Li_2TiO_3 promotes the interfacial decomposition of $LiPF_6$ and facilitates the formation of a uniform LiF-rich passivation layer[45]. The N 1s spectrum in Supplementary Figure 16B reveals the presence of Li_3N in addition to LiF within the SEI layer, which may originate from the decomposition of imidazole ligands in ZIF-67. At the interface, Co (II) sites act as Lewis acid centers, facilitating the cleavage of imidazole rings and promoting the formation of Li_3N[46]. The LiF/Li_3N interlayer exhibits high Li^+ conductivity while simultaneously providing a mechanically robust barrier to effectively inhibit dendrite growth. To investigate the potential influence of these interfacial decomposition reactions, the distribution of Co species within the SEI layer was further analyzed. As shown in Supplementary Figure 16C, no Co signal was detected in the anodic SEI layer, indicating that the interfacial reactions do not induce dissolution of Co from ZIF-67. As discussed above, maintaining the Co (II) state not only contributes to the structural stability of the interface but also facilitates the stable generation of Li_3N.

The QSSE was further examined after 800 h of cycling to validate the long-term stability of the BC/ZIF-67@Li_2TiO_3 electrolyte. Supplementary Figure 17 presents the XRD patterns of the electrolyte before and after cycling. All characteristic diffraction peaks corresponding to BC and ZIF-67 remain well indexed

after cycling. Although partial decomposition of the imidazole ligands occurs at the interface [Supplementary Figure 16B], this process does not affect the overall crystal structure of BC/ZIF-67@Li_2TiO_3 during long-term cycling.

As shown in Supplementary Figure 18, SEM analysis reveals that the electrolyte framework remains intact without any apparent structural collapse, maintaining its characteristic crosslinked network architecture. To further assess the microstructural integrity, HAADF-STEM images were collected after cycling [Supplementary Figure 19]. The morphology of BC/ZIF-67@Li_2TiO_3 remains highly stable even after 800 h of operation, with the ZIF-67 framework still clearly distinguishable. Furthermore, EDS mapping confirms that all constituent elements (Ti, C, N, Co, and O) retain a uniform spatial distribution. No obvious aggregation of Co species (from ZIF-67) or Ti species (from Li_2TiO_3) is detected within the composite structure, further demonstrating the excellent structural and chemical stability of the hybrid electrolyte.

XAFS analysis was further conducted to investigate the evolution of the local structure around Co sites in the electrolyte before and after electrochemical cycling. The Co K-edge X-ray absorption near-edge structure (XANES) spectra of ZIF-67, BC/ZIF-67, and ZIF-67@Li_2TiO_3 under different states are presented in Figure 4I and Supplementary Figure 20A. As shown in Supplementary Figure 20B, the valence state of Co remains nearly unchanged before and after cycling, demonstrating the excellent chemical stability of the electrolyte during electrochemical operation. However, the white-line peak intensity in the energy-space spectra reveals that the local coordination environment of Co, particularly the Co-N and Co-O coordination structures, undergoes subtle changes after cycling. This phenomenon is mainly attributed to the interaction between Li^+ and the active sites within ZIF-67. The coordination of Li^+ weakens the interaction between Co and N atoms, resulting in localized structural rearrangement around the Co centers, which is further supported by the Fourier-transformed EXAFS spectra in Figure 4J. The first coordination shell exhibits a noticeable shift toward higher R-space values, confirming the expansion of the local coordination sphere induced by Li^+ coordination. Moreover, the enhanced white-line intensity after cycling suggests the formation of a more ordered local structure within BC/ZIF-67@Li_2TiO_3. This phenomenon can also be attributed to microscopic structural adjustments induced by Li^+ coordination, which lead to a more regular Co coordination environment. Such an increased degree of structural ordering is beneficial for efficient ion transport throughout the electrolyte matrix[47]. To further elucidate the local coordination structure of Co (II), wavelet transform (WT) analyses of the k^3-weighted EXAFS signals for the BC/ZIF-67@Li_2TiO_3 electrolyte before and after 800 h of cycling are presented in Figure 4K. The contour plot of the BC/ZIF-67@Li_2TiO_3 electrolyte after 800 h of cycling exhibits maximum intensity at approximately 1.5 Å. The slight variation in the high-k region is attributed to changes in the Co-N coordination environment induced by the bridging interactions between BC and Li^+.

Based on the above analyses, we confirm that the outstanding electrochemical performance of the BC/ZIF-67@Li_2TiO_3 electrolyte primarily originates from the synergistic effects of the ZIF-67 bridging strategy and α-Li_2TiO_3 incorporation. The bridging effect of ZIF-67 optimizes the organic-inorganic interface structure, while the introduction of α-Li_2TiO_3 establishes rapid Li^+ transport pathways, thereby accelerating Li^+ conduction throughout the electrolyte framework. More importantly, as a Li^+ conductor, α-Li_2TiO_3 selectively facilitates Li^+ migration and suppresses anion transport within the electrolyte, leading to an increased t_{Li+}. This conclusion is consistent with the results presented in Figure 3B. Beyond its role as an active ionic-conductive filler, the post-cycling analysis of lithium anodes reveals a new interaction between α-Li_2TiO_3 and lithium dendrites, which is defined herein as the "tip-shielding effect". This effect originates from the interfacial reaction between α-Li_2TiO_3 and lithium dendrites, providing an additional active defense mechanism against dendrite propagation.

To elucidate the tip-shielding effect of α-Li_2TiO_3, a non-electrochemical static reaction experiment was conducted between lithium metal and α-Li_2TiO_3. Specifically, a 16 mm lithium disk was assembled with 0.05 g α-Li_2TiO_3 powder in a coin cell to ensure intimate contact, followed by static heating at 80 °C. The inset images show the morphology of lithium metal before and after the reaction. The results indicate that the lithium surface becomes roughened after reaction, suggesting the occurrence of interfacial chemical transformation. The corresponding changes in valence states were further evaluated by XPS. In Supplementary Figure 21A, the Ti 2p XPS spectrum can be assigned to Ti^{4+} (464.35 and 458.5 eV), Ti^{3+} (463.72 and 457.87 eV), and Ti^{2+} (461.2 and 455.9 eV) species[48,49]. This means that the titanium from the α-Li_2TiO_3 (+4) is being reduced to Ti^{2+} and Ti^{3+} by lithium. Meanwhile, lithium metal undergoes oxidation during this process. In Supplementary Figure 21B, the Li 1s spectrum exhibits a peak at 53.6 eV, corresponding to Li_2O [50], while the signal at 57.8 eV originates from Ti 3s. In addition, small amounts of LiOH and Li_2CO_3 are detected. These results provide direct evidence that when lithium dendrites contact α-Li_2TiO_3, lithium is oxidized into lithium-containing oxide species. The overall reaction can be expressed as $Li + Li_2TiO_3 \rightarrow Li_xO + TiO_x$. This interfacial reaction provides a new strategy for designing active-defense electrolytes capable of dynamically regulating lithium dendrite growth.

To further visualize lithium dendrite evolution and verify the proposed tip-shielding effect, Li-Cu asymmetric cells were constructed using BC/ZIF-67 and BC/ZIF-67@Li_2TiO_3 as QSSEs, respectively. Lithium deposition was controlled by adjusting the deposition time at a current density of 1 mA cm^{-2}. Figure 5A and B presents ex situ SEM images obtained after different deposition times. The results show that the amount of lithium deposition on the Cu electrode surface increases gradually with prolonged deposition time. For the BC/ZIF-67 system [Figure 5A], lithium growth occurs without effective regulation, exhibiting a strong tendency toward out-of-plane accumulation. After 8 h of deposition, a large amount of irregular lithium deposits accumulates on the electrode surface, resulting in increased surface roughness. In contrast, lithium deposition in the BC/ZIF-67@Li_2TiO_3 system [Figure 5B] is more regulated. Lithium preferentially grows laterally along the Cu substrate surface rather than forming vertically extended dendrites. This behavior can be attributed to two factors. First, the continuous Li^+ transport pathways within the BC/ZIF-67@Li_2TiO_3 framework facilitate uniform ion distribution across the electrode surface, preventing localized Li^+ accumulation and suppressing dendrite nucleation. Second, the tip-shielding effect restricts the vertical extension of lithium growth, thereby directing lithium deposition toward a more uniform horizontal growth mode.

It is noteworthy that the tip-shielding effect originates from the reduction reaction of Li_2TiO_3, which could potentially influence the long-term stability of the electrolyte. To address this concern, the phase evolution of the electrolyte after prolonged cycling was systematically investigated. Supplementary Figure 17 presents the XRD patterns of the electrolyte before and after cycling. The characteristic diffraction peaks at 43° and 64° are assigned to Li_2TiO_3. After cycling, these diffraction peaks remain clearly visible, indicating that the bulk Li_2TiO_3 phase is well preserved. This evidence demonstrates that the tip-shielding mechanism is confined to the localized electrolyte/dendrite interface and does not compromise the structural integrity of the bulk electrolyte. Therefore, the proposed tip-shielding strategy does not result in excessive consumption of Li_2TiO_3.

Although the above results confirm the effectiveness of the tip-shielding effect, direct evidence of its dynamic evolution during dendrite growth remains lacking. Therefore, an *in situ* microscopic observation experiment was designed to simulate dendrite growth and visualize the tip-shielding process. As directly observed in Figure 5C and Supplementary Figure 22, the real-time deposition process clearly demonstrates the suppression of dendritic growth. In both systems, dendrites gradually extend toward the electrode surface as deposition proceeds. After 40 min, when dendrites reach the BC/ZIF-67 electrolyte, the discharge curve

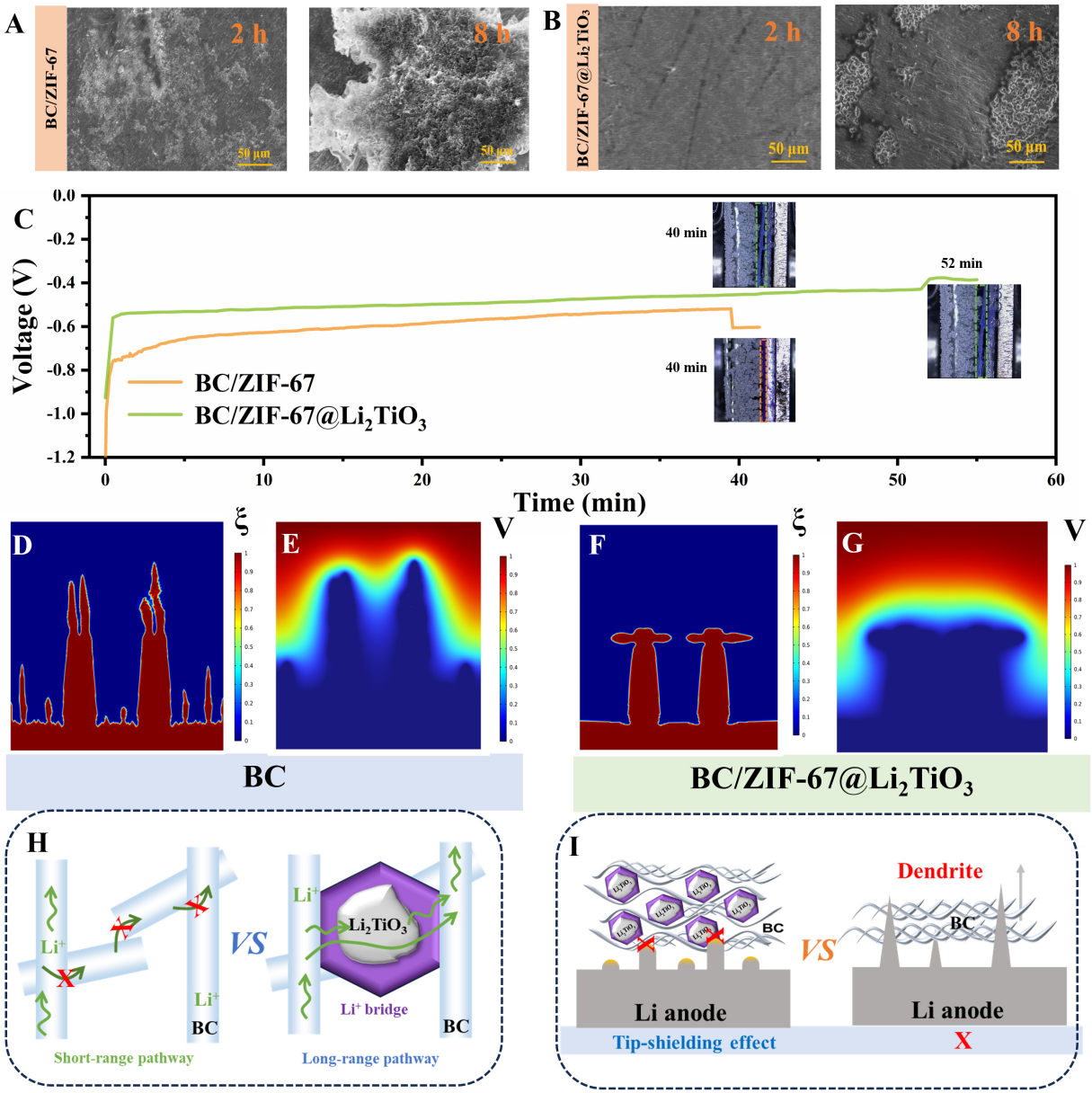

Figure 5. Mechanism research. (A and B) SEM images of lithium deposition morphology on the copper surface of the Li||Cu battery at different deposition times at 1 mA cm^{-2}; (C) Single-cycle galvanostatic discharge profiles of BC/ZIF-67 and BC/ZIF-67@Li_2TiO_3 QSSEs at 10 mA cm^{-2}; inset shows *in situ* optical microscopy images of electrolyte-electrode interfaces; (D and E) BC QSSE and (F and G) BC/ZIF-67@Li_2TiO_3 QSSE lithium dendrite growth simulation; (H) Schematic diagram of the bridging effect of ZIF-67; (I) Schematic diagram of the tip-shielding effect of Li_2TiO_3. BC: Bacterial cellulose; ZIF-67: zeolitic imidazolate framework-67; QSSEs: quasi-solid-state electrolytes; SEM: scanning electron microscope.

begins to fluctuate, indicating that dendrite penetration through the separator has occurred. In contrast, when dendrites reach the BC/ZIF-67@Li_2TiO_3 electrolyte after 40 min, the curve remains stable. Obvious voltage fluctuations only appear after 52 min, suggesting that BC/ZIF-67@Li_2TiO_3 can react with dendrite tips and effectively prolong battery operation. It should be noted that a higher current density was applied in this experiment to accelerate dendrite growth and obtain observable dynamic behavior.

Building upon these experimental observations, a phase-field simulation was further constructed to elucidate the mechanism by which the "tip-shielding effect" provides active protection against lithium dendrites. The key parameters and calculation conditions are summarized in Supplementary Table 1. As shown in

Figure 5D-G and Supplementary Figure 23, a time-dependent electrochemical-mechanical phase-field model was employed to simulate the evolution of lithium dendrite growth. As presented in Supplementary Figure 23A-C, in the battery system employing BC as the electrolyte, lithium dendrites initially exhibit a needle-like morphology. With prolonged simulation time, lithium deposition gradually develops into larger dendritic structures, as illustrated in Supplementary Figure 23D-F. Ultimately, as shown in Figure 5D and E, the uncontrolled dendrite growth can be attributed to the insufficient interfacial stress between lithium dendrites and the BC matrix, which cannot effectively suppress dendrite propagation, together with the continuous accumulation of Li^+ concentration during deposition. In contrast, the lithium dendrite growth behavior in the BC/ZIF-67@Li_2TiO_3 electrolyte differs from that in the pristine BC electrolyte. As illustrated in Supplementary Figure 23J-L, the dendrite growth mode undergoes an obvious transition. Upon contacting α-Li_2TiO_3, an *in situ* oxide passivation layer forms at the dendrite tips, which effectively redirects the subsequent lithium deposition pathway. Consequently, as demonstrated by the simulation results in Figure 5F and G, lithium dendrites transition from vertical propagation to lateral growth. This simulated behavior agrees well with the experimental observations in Figure 5, further confirming the beneficial role of the tip-shielding effect.

In summary, the combined experimental results and theoretical simulations confirm the superior electrochemical performance of the BC/ZIF-67@Li_2TiO_3 electrolyte and clarify the underlying enhancement mechanism. The electrolyte exhibits high ionic conductivity and an increased t_{Li+}, primarily owing to the bridging function of ZIF-67 within the composite matrix. This interconnected structure establishes long-range and continuous Li^+ transport pathways. Based on the above discussion, the schematic mechanism of the ZIF-67 bridging effect is illustrated in Figure 5H. For the BC electrolyte, although abundant polar functional groups exist on the cellulose surface, the high crystallinity of cellulose limits effective fiber connectivity, which relies mainly on weak intermolecular interactions. Consequently, Li^+ migration is restricted to localized regions. After introducing ZIF-67, the MOF structure acts as a bridge to chemically connect cellulose fibers with inorganic fillers, constructing a three-dimensional interconnected network. This architecture enhances Li^+ conduction across different phases. Through these bridges, Li^+ migration pathways are extended throughout the bulk electrolyte, resulting in reduced E_a. Furthermore, the enhanced ion-transport kinetics promote a more homogeneous Li^+ distribution at the anode surface, thereby effectively suppressing lithium dendrite growth. Figure 5I illustrates the proposed "tip-shielding effect". As discussed above, this mechanism differs fundamentally from traditional strategies based on rigid interphase construction. Rather than relying on high mechanical strength to physically block dendrite penetration, the tip-shielding effect utilizes an interfacial chemical reaction to actively passivate dendrite tips. This approach transforms dendrite suppression from a passive mechanical barrier strategy into an active chemical regulation strategy, thereby enabling excellent long-term cycling stability of lithium metal batteries.

Full-cell performance

To evaluate the practical applicability of the QSSE in full-cell configurations, $LiNi_{0.8}Co_{0.1}Mn_{0.1}O_2$ (NCM) was employed as the cathode with a mass loading of approximately 5.7 mg cm^{-2}. The detailed full-cell parameters are summarized in Supplementary Table 2. Galvanostatic tests were performed at 25 °C. Compared with the BC and BC/ZIF-67 electrolytes, the Li||NCM battery employing the BC/ZIF-67@Li_2TiO_3 electrolyte exhibited superior rate capability and capacity performance. Specifically, it delivered high specific capacities of 170.6 mAh g^{-1} (0.97 mAh cm^{-2}) and 136.3 mAh g^{-1} (0.78 mAh cm^{-2}) at 2 C and 5 C with a voltage window of 2.8-4.5 V, respectively [Figure 6A and B]. When the current density was returned to 0.2 C, the capacity rapidly recovered, demonstrating the excellent structural stability of the BC/ZIF-67@Li_2TiO_3 electrolyte during repeated high-rate charge/discharge processes. The improved high-rate performance can be attributed to the excellent electrochemical compatibility of the QSSE within the wide operating voltage window of the Li|BC/ZIF-67@Li_2TiO_3|NCM battery. During charge and discharge processes, Li^+ ions interact

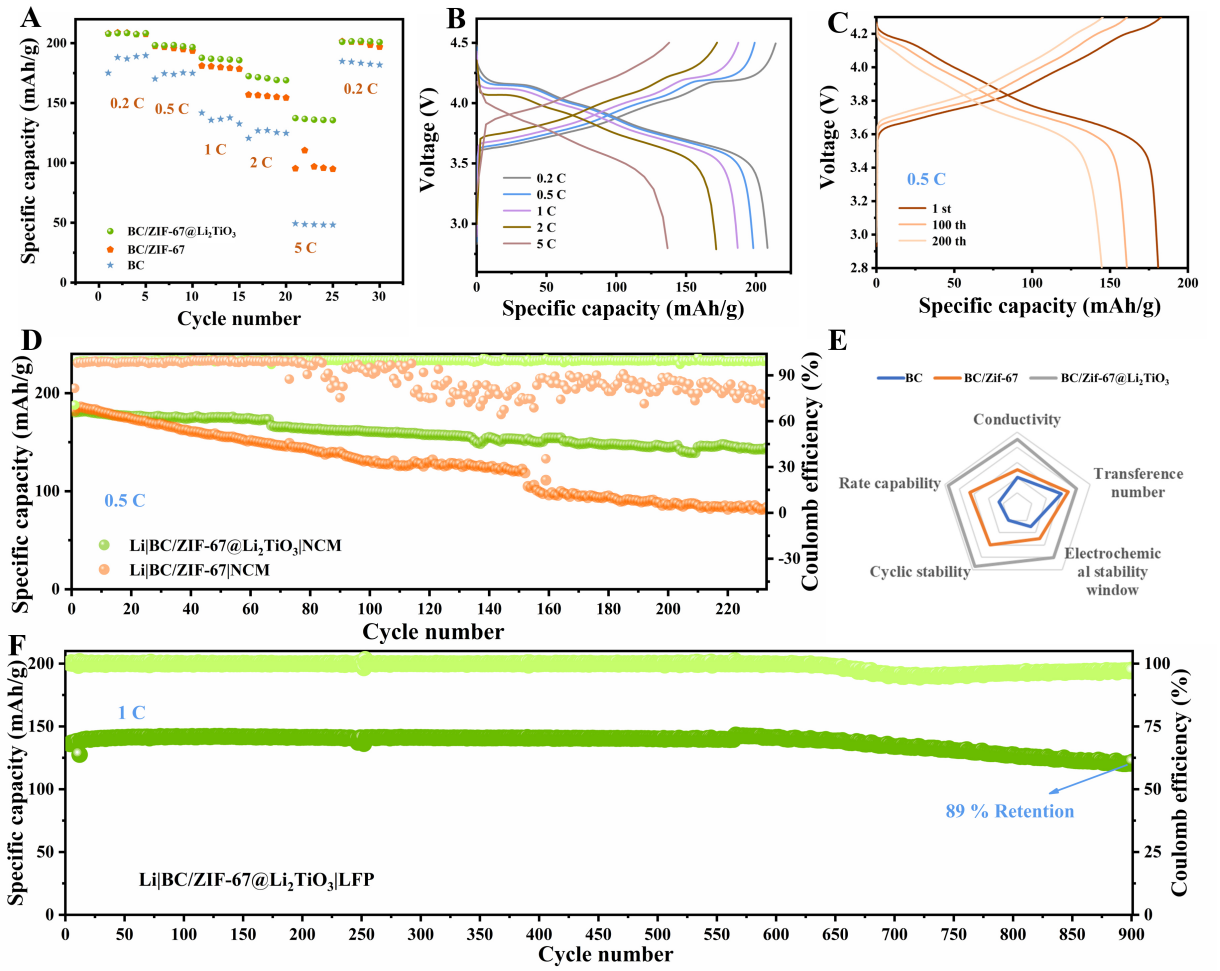

Figure 6. The electrochemical performances of full cells. (A) Rate performance of Li||NCM cells and (B) the corresponding voltage profiles of the Li|BC/ZIF-67@Li_2TiO_3|NCM cell at different rates; (C) Voltage profiles and (D) cycling performance of Li|BC/ZIF-67@Li_2TiO_3 and Li|BC/ZIF-67|NCM cells measured at 0.5 C; (E) Performance comparison in terms of conductivity, cyclic stability, rate capability, transference number, and electrochemical stability window (ESW); (F) Cycling performance of Li|BC/ZIF-67@Li_2TiO_3|LFP battery at 1 C. BC: Bacterial cellulose; ZIF-67: zeolitic imidazolate framework-67; NCM: $LiNi_{0.8}Co_{0.1}Mn_{0.1}O_2$; LFP: $LiFePO_4$.

primarily with oxygen-containing functional groups on the cellulose surface and coordination sites within ZIF-67. Through coordination with polar functional groups or pore structures, Li^+ undergoes a reversible coordination-dissociation process, which facilitates ion transport between molecular chains and enhances ionic conductivity. Furthermore, incorporating open-layered α-Li_2TiO_3 into the QSSE establishes well-defined pathways for reversible Li^+ intercalation and deintercalation. This structural configuration promotes efficient intralayer Li^+ migration, thereby regulating lithium deposition, suppressing dendrite growth, and improving the overall electrochemical performance of the battery. Subsequently, long-term cycling tests of the full cells were conducted at 0.5 C with a voltage range of 2.8-4.3 V. As shown in Figure 6C and D, the Li|BC/ZIF-67@Li_2TiO_3|NCM cell delivered an initial discharge capacity of 180.2 mAh g^{-1} (1.03 mAh cm^{-2}) at 0.5 C. After 200 charge/discharge cycles, the cell maintained a capacity retention above 80%. In contrast, the Li|BC/ZIF-67|NCM cell exhibited a lower capacity retention of only 45.6%. To further demonstrate the comprehensive performance of the designed electrolyte system, a radar chart was constructed to compare five key performance metrics [Figure 6E].

Meanwhile, long-term cycling tests were also conducted at room temperature using Li||$LiFePO_4$ (LFP) full cells assembled with BC/ZIF-67 and BC/ZIF-67@Li_2TiO_3 QSSEs under a voltage window of 2.5-4.2 V at 25 °C [Supplementary Figure 24]. After 100 cycles at 0.5 C, the Li|BC/ZIF-67@Li_2TiO_3|LFP cell maintained a

discharge capacity of 157 mAh g^{-1} (0.4 mAh cm^{-2}) with a Coulombic efficiency of 97.6%, whereas the Li|BC/ZIF-67|LFP cell delivered a capacity of 151 mAh g^{-1} (0.38 mAh cm^{-2}) with a lower Coulombic efficiency of 93.7%. As shown in Figure 6F, the Li|BC/ZIF-67@Li_2TiO_3|LFP cell also exhibited outstanding long-term cycling stability over 900 cycles at 1 C with an active material loading of ~2.5 mg cm^{-2}. During this extended cycling process, the cell retained 89% of its initial capacity, corresponding to a reversible capacity of 121.2 mAh g^{-1}. This excellent cycling performance demonstrates that the incorporation of Li_2TiO_3 effectively suppresses lithium dendrite formation and improves the long-term stability of the battery. Overall, the prepared BC/ZIF-67@Li_2TiO_3 QSSE exhibits a high t_{Li+}, excellent ionic conductivity, a wide electrochemical stability window, and outstanding cycling durability, outperforming previously reported cellulose-based QSSE systems. This structural design strategy provides a promising new direction for the development of advanced QSSEs.

To further compare the performance of the proposed electrolyte with previously reported QSSE systems, a summary of cellulose-based electrolytes from the literature was compiled [Supplementary Table 3]. Most reported studies utilize MOFs as active fillers to enhance Li^+ conductivity. In contrast, this work represents the first attempt to employ MOFs as ion bridges to connect BC and α-Li_2TiO_3, thereby reducing unfavorable interfacial impedance and constructing continuous Li^+ transport pathways. This unique structural design results in high t_{Li+} and enhanced ionic conductivity. Furthermore, as summarized in Supplementary Table 3, the BC/ZIF-67@Li_2TiO_3 electrolyte achieves an extended cycling lifetime, which can be attributed to the proposed tip-shielding effect.

Although the electrolyte developed in this work demonstrates superior performance in coin-type full cells compared with previously reported systems and shows promising application potential, further optimization is still required for large-capacity batteries with higher cathode loadings. Supplementary Figure 25 presents preliminary evaluation results of pouch cells employing an NCM811 cathode. Although the pouch cell demonstrates encouraging electrochemical performance, further systematic investigations into cell fabrication processes and optimization strategies are necessary. For practical high-loading cathodes, prolonged Li^+ diffusion pathways and increased polarization under high areal loading remain major challenges. Therefore, electrolyte thickness, pore architecture, and spatial distribution of fillers should be further optimized to enable compatibility with high-loading electrodes and facilitate the development of high-energy-density lithium metal batteries.

CONCLUSIONS

In summary, a hybrid QSSE has been successfully developed by employing cellulose as the structural framework, α-Li_2TiO_3 as the active filler, and ZIF-67 as an ion-bridging component to construct continuous lithium-ion transport pathways. The vacuum filtration method used for fabrication is simple, controllable, and compatible with industrial papermaking and roll-to-roll manufacturing processes, demonstrating potential for large-scale production. The resulting BC/ZIF-67@Li_2TiO_3 electrolyte exhibits outstanding electrochemical performance and provides a new strategy for establishing long-range Li^+ transport pathways through an effective bridging effect. The main conclusions can be summarized from three aspects:

(1) The bridging effect of ZIF-67 successfully integrates localized ion-conduction regions within the BC matrix and enhances interfacial compatibility between BC and Li_2TiO_3, thereby constructing continuous long-range Li^+ transport pathways. As a result, the hybrid electrolyte achieves a high ionic conductivity of 2.3 × 10^{-3} S cm^{-1} and an exceptionally high t_{Li+} of 0.81. Meanwhile, the electrochemical stability window is extended from 4.9 V to 5.4 V.

(2) The innovative incorporation of low-temperature α-Li_2TiO_3 provides dual functionality within the electrolyte system. As an active inorganic filler, it contributes to enhanced ionic conductivity and improved Li^+ selectivity. Meanwhile, multi-physics simulations and electrochemical analyses confirm that α-Li_2TiO_3 induces a tip-shielding effect and regulates ion distribution, thereby effectively suppressing lithium dendrite formation.

(3) The BC/ZIF-67@Li_2TiO_3 hybrid electrolyte demonstrates considerable potential for practical applications, exhibiting excellent stability in various full-cell configurations. The Li|BC/ZIF-67@Li_2TiO_3|LFP battery maintains a capacity retention of 89% after 900 cycles at 1 C. Furthermore, the Li|BC/ZIF-67@Li_2TiO_3|NCM battery delivers an initial discharge capacity of 180.2 mAh g^{-1} at 0.5 C at room temperature and retains 80% of its capacity after 200 cycles. These results highlight the excellent compatibility of the developed electrolyte with both high-safety and high-energy-density cathode systems.

DECLARATIONS

Acknowledgments

Allocation of beamtime at 4W1A (31109.02.BSRF.4W1A) and 4B9B (31109.02.BSRF.4B9B), BSRF, Beijing, China, is gratefully acknowledged.

Authors' contributions

Methodology, investigation, and manuscript writing: Chu, D.; Gao, R.; Hu, L.; Xu, H.
Performed data acquisition: Xu, H.; Yang, D.; Gao, Z.; Huang, W.
Project administration and funding acquisition: Gao, R.; Feng, M.
Conceptualization and supervision: Chu, D.; Gao, R.; Chen, Z.

Availability of data and materials

The original contributions presented in this study are included in the article/Supplementary Materials. Further inquiries can be directed to the corresponding authors.

AI and AI-assisted tools statement

Not applicable.

Financial support and sponsorship

This research was funded by the Scientific and Technological Innovation Project of Changbaishan Laboratory, Jilin Province (Grant No. CBS2025003-01), the National Natural Science Foundation of China (Grant No. 52471229), and the Fundamental Research Funds for the Central Universities (No. 2025MS014).

Conflict of interests

All authors declared that there are no conflicts of interest.

Ethical approval and consent to participate

Not applicable.

Consent for publication

Not applicable.

Supplementary Materials

Supplementary Materials

REFERENCES

1. Wang, J.; Zhang, J.; Cheng, X.; et al. Electrode/electrolyte interface studies of rechargeable Li batteries with interface-specific sum frequency generation spectroscopy. *J. Am. Chem. Soc.* **2025**, *147*, 44633-51. DOI
2. Wang, J.; Tang, B.; Wu, J.; et al. Revitalizing dendritic lithium with atomic modulator-decorated suspension electrolyte for durable lithium metal batteries. *Sci. Adv.* **2026**, *12*, eaef9111. DOI PubMed PMC
3. Zhang, J.; Liu, F.; He, R.; et al. Taming interfacial ion-dipole interactions with d-orbital delocalized electron catalysis expediates low-temperature Li metal batteries. *Adv. Mater.* **2026**, *38*, e10894. DOI
4. Zhang, Z.; Han, W. From liquid to solid-state lithium metal batteries: fundamental issues and recent developments. *NanoMicro. Lett.* **2024**, *16*, 24. DOI PubMed PMC
5. Jiang, Z.; Chen, S.; Wei, C.; et al. Enabling superior electrochemical performance of NCA cathode in $Li_{5.5}PS_{4.5}Cl_{1.5}$-based solid-state batteries with a dual-electrolyte layer. *Chin. Chem. Lett.* **2024**, *35*, 108561. DOI
6. Nguyen, M. H.; Niu, C.; Ngo, N. M.; Chen, J.; Park, S. Recent progress on metal-organic framework-based separators for quasi-solid-state lithium metal batteries. *Energy. Mater.* **2025**, *5*, 500093. DOI
7. Hou, Y.; Chen, Z.; Zhang, R.; Cui, H.; Yang, Q.; Zhi, C. Recent advances and interfacial challenges in solid-state electrolytes for rechargeable Li-air batteries. *Exploration* **2023**, *3*, 20220051. DOI
8. Chen, G.; Liu, X.; Liu, Z.; et al. Novel "sandwich" configuration with ALD-coating layers on electrode/electrolyte interfaces for durable all-solid-state lithium metal batteries with high-voltage cathodes. *Energy. Mater.* **2025**, *5*, 500064. DOI
9. Park, G.; Jeon, D. W.; Jang, I.; et al. Investigation of the effects of heteroatom doping on von-Alpen-type NASICON electrolytes and its applications to solid-state sodium batteries. *J. Adv. Ceram.* **2025**, *14*, 9221138. DOI
10. Zhang, A.; Bi, Z.; Yang, E.; et al. Formulating electrophilic electrolyte for in situ stabilization of 4.8 V Li-Rich batteries with 100% initial coulombic efficiency. *Angew. Chem. Int. Ed.* **2025**, *64*, e202502603. DOI
11. Zhou, X.; Chang, C. Y.; Yu, D.; et al. Li_2ZrF_6 protective layer enabled high-voltage $LiCoO_2$ positive electrode in sulfide all-solid-state batteries. *Nat. Commun.* **2025**, *16*, 112. DOI PubMed PMC
12. Zhang, Y.; Liu, H.; Liu, F.; et al. Dual-anion-rich polymer electrolytes for high-voltage solid-state lithium metal batteries. *ACS. Nano.* **2025**, *19*, 3197-209. DOI
13. Yu, T.; Liu, Y.; Li, H.; Sun, Y.; Guo, S.; Zhou, H. Ductile inorganic solid electrolytes for all-solid-state lithium batteries. *Chem. Rev.* **2025**, *125*, 3595-662. DOI
14. Jiang, Z.; Peng, H.; Liu, Y.; et al. A Versatile $Li_{6.5}In_{0.25}P_{0.75}S_5I$ sulfide electrolyte triggered by ultimate-energy mechanical alloying for all-solid-state lithium metal batteries. *Adv. Energy. Mater.* **2021**, *11*, 2101521. DOI
15. Shin, S.; Kang, S. H.; Kim, G.; et al. Intergranular amorphous film in GeO_2-enriched $Li_{1.5}Al_{0.5}Ti_{1.5}(PO_4)_3$ composite electrolytes for high-performance solid-state lithium-ion batteries. *Composites. Part. B.* **2024**, *280*, 111478. DOI
16. He, C.; Ying, H.; Cai, L.; et al. Tailoring stable PEO-based electrolyte/electrodes interfaces via molecular coordination regulating enables 4.5 V solid-state lithium metal batteries. *Adv. Funct. Mater.* **2024**, *34*, 2410350. DOI
17. Xu, H.; Liu, S.; Li, Z.; et al. Synergistic effect of $Ti_3C_2T_x$ MXene/PAN nanofiber and LLZTO particles on high-performance PEO-based solid electrolyte for lithium metal battery. *J. Colloid. Interface. Sci.* **2024**, *668*, 634-45. DOI
18. Zhang, X.; Cheng, S.; Fu, C.; et al. Advancements and challenges in organic-inorganic composite solid electrolytes for all-solid-state lithium batteries. *NanoMicro. Lett.* **2024**, *17*, 2. DOI
19. Chen, P.; Ding, B.; Dou, H.; Zhang, X. Ceramic-polymer composite solid-state electrolytes for solid-state lithium metal batteries: mechanism, strategy, and prospect. *Small* **2025**, *21*, e2503743. DOI PubMed
20. Deng, Y.; Zhu, T.; Cheng, Y.; et al. Recent advances in functional cellulose-based materials: classification, properties, and applications. *Adv. Fiber. Mater.* **2024**, *6*, 1343-68. DOI
21. Kim, H.; Lee, C.; Jo, J.; et al. Multilayered separators with core-shell structured nanocellulose-SiO_2 nanocomposites for lithium-ion batteries. *Carbohydr. Polym.* **2025**, *362*, 123677. DOI
22. Wang, R.; Dong, W.; Song, Z.; et al. Ion-conducting molecular-grafted sustainable cellulose quasi-solid composite electrolyte for high stability solid-state lithium-metal batteries. *Adv. Funct. Mater.* **2024**, *34*, 2402461. DOI
23. Xu, Y.; Guo, Y.; Zhang, X.; et al. Tailoring highly ion-conductive and stabled PVDF-based solid electrolyte via surface coordination chemistry. *Adv. Funct. Mater.* **2025**, *35*, 2422461. DOI
24. Cao, W.; Zhang, K.; Wang, J.; et al. Self-assembled silica-cellulose-ether ternary nanocomposite electrolytes for robust quasi-solid-state lithium metal batteries. *Energy. Storage. Mater.* **2025**, *75*, 104067. DOI
25. Liu, Y.; Yu, Y.; Liu, Y.; et al. Biobased polymer electrolyte with plant cell wall-inspired architecture: biomimetic integration of cellulose-lignin for nonflammable cryogenic lithium batteries. *Adv. Energy. Mater.* **2025**, *15*, 2501737. DOI
26. Mo, S.; An, H.; Liu, Q.; et al. Multistage bridge engineering for electrolyte and interface enables quasi-solid batteries to operate at -40 °C. *Energy. Storage. Mater.* **2024**, *65*, 103179. DOI

27. Zhu, F.; Wang, J.; Zhang, Y.; et al. Low-temperature lithium metal batteries achieved by synergistically enhanced screening Li^+ desolvation kinetics. *Adv. Mater.* **2025**, *37*, e2411601. DOI
28. Zheng, Y.; Yang, N.; Gao, R.; et al. "Tree-Trunk" design for flexible quasi-solid-state electrolytes with hierarchical ion-channels enabling ultralong-life lithium-metal batteries. *Adv. Mater.* **2022**, *34*, e2203417. DOI
29. Cheng, L.; Zhang, Y.; Li, D.; et al. Cu-MOF functionalized hydroxyapatite/bacterial cellulose composite separator enabling dendrite-free fast charging and enhanced thermal safety for high-loading graphite anode. *Adv. Funct. Mater.* **2026**, *36*, e15523. DOI
30. Lin, R.; Jin, Y.; Zhang, X.; Li, Y.; Zhang, Y.; Xiong, Y. Hierarchical bulk-interface design of MOFs framework for polymer electrolyte towards ultra-stable quasi-solid-state Li metal batteries. *Chem. Eng. J.* **2024**, *479*, 147558. DOI
31. Zhou, Q.; Oya, Y.; Chikada, T.; Zhang, W.; Xue, L.; Yan, Y. Preparation of Li_2TiO_3 by hydrothermal synthesis and its structure evolution under high energy Ar^+ irradiation. *J. Eur. Ceram. Soc.* **2017**, *37*, 4955-61. DOI
32. Sun, X.; Xu, W.; Zhang, X.; Lei, T.; Lee, S.; Wu, Q. ZIF-67@Cellulose nanofiber hybrid membrane with controlled porosity for use as Li-ion battery separator. *J. Energy. Chem.* **2021**, *52*, 170-80. DOI
33. Xu, Y.; Chen, Z.; Wang, J.; et al. Design of quasi-metal-organic frameworks for solid polymer electrolytes enabling an ultra-stable interface with Li metal anode. *Angew. Chem. Int. Ed.* **2025**, *64*, e202416170. DOI
34. Wu, X.; Liu, W.; Wu, H.; et al. Nanoporous ZIF-67 embedded polymers of intrinsic microporosity membranes with enhanced gas separation performance. *J. Membrane. Sci.* **2018**, *548*, 309-18. DOI
35. Wang, F.; Kim, H.; Park, S.; Kee, C.; Kim, S.; Oh, I. Bendable and flexible supercapacitor based on polypyrrole-coated bacterial cellulose core-shell composite network. *Compos. Sci. Technol.* **2016**, *128*, 33-40. DOI
36. Xu, T.; Du, H.; Liu, H.; et al. Advanced nanocellulose-based composites for flexible functional energy storage devices. *Adv. Mater.* **2021**, *33*, e2101368. DOI
37. Zou, J.; Dong, H.; Wu, H.; et al. Laser-induced rapid construction of Co/N-doped honeycomb-like carbon networks as oxygen electrocatalyst used in zinc-air batteries. *Carbon* **2022**, *200*, 462-71. DOI
38. Liu, P.; Xiao, L.; Chen, Y.; Chen, H. Highly enhanced electrochemical performances of $LiNi_{0.815}Co_{0.15}Al_{0.035}O_2$ by coating via conductively $LiTiO_2$ for lithium-ion batteries. *Ceram. Int.* **2019**, *45*, 18398-405. DOI
39. Xie, Y.; Wang, Q.; Gu, F.; Dai, K.; Shui, M.; Shu, J. The electro-chemical properties and intercalation mechanism of low strain Li_2TiO_3 as a high-performance anode material for lithium-ion batteries. *J. Alloys. Compd.* **2022**, *893*, 162348. DOI
40. Sun, X.; Sun, S.; Gu, S.; et al. High-performance single atom bifunctional oxygen catalysts derived from ZIF-67 superstructures. *Nano. Energy.* **2019**, *61*, 245-50. DOI
41. Gao, Q.; Li, J.; He, Y.; et al. High-performance antioxidant behavior of zeolitic imidazolate framework-67 at low filler content in silicone rubber. *Polym. Degrad. Stabil.* **2021**, *190*, 109622. DOI
42. Zhu, W.; Zhang, L.; Liu, S.; et al. Enhanced CO_2 electroreduction on neighboring Zn/Co monomers by electronic effect. *Angew. Chem. Int. Ed.* **2020**, *59*, 12664-8. DOI
43. Yuan, B.; Cong, Z.; Cheng, Z.; et al. Bacteria cellulose framework-supported solid composite polymer electrolytes for ambient-temperature lithium metal batteries. *Nanotechnology* **2022**, *33*, 415401. DOI
44. Song, X.; Ma, K.; Wang, J.; et al. Three-dimensional metal-organic framework@cellulose skeleton-reinforced composite polymer electrolyte for all-solid-state lithium metal battery. *ACS. Nano.* **2024**, *18*, 12311-24. DOI
45. Brown, Z. L.; Jurng, S.; Nguyen, C. C.; Lucht, B. L. Effect of fluoroethylene carbonate electrolytes on the nanostructure of the solid electrolyte interphase and performance of lithium metal anodes. *ACS. Appl. Energy. Mater.* **2018**, *1*, 3057-62. DOI
46. Li, L.; Wang, Z.; Li, H.; et al. ZIF-67 decorated PVDF fibers embedded in PEO and infiltrated with ionic liquid as composite polymer electrolyte for high performance secondary batteries using lithium metal as anode. *J. Energy. Storage.* **2025**, *124*, 116932. DOI
47. Patil, R.; Kumar, N.; Bhattacharjee, S.; et al. Influence of catalase encapsulation on cobalt@nanoporous carbon with multiwall shell for supercapacitor and polyurethane synthesis using carbon dioxide. *Chem. Eng. J.* **2023**, *453*, 139874. DOI
48. Wang, Y.; Liu, H.; Shi, Q.; et al. Single-atom titanium on mesoporous nitrogen, oxygen-doped carbon for efficient photo-thermal catalytic CO_2 cycloaddition by a radical mechanism. *Angew. Chem. Int. Ed.* **2024**, *63*, e202404911. DOI
49. Wang, R.; Yang, G.; Yang, T.; et al. Superionic conduction electrolyte through in situ structural transformation in electrochemical cell. *Commun. Mater.* **2025**, *6*, 811. DOI
50. Santos, ÉA.; Policano, M. C.; Pinzón, M. J.; et al. Operando FTIR study on water additive in lithium-sulfur batteries to mitigate shuttle effect. *J. Energy. Chem.* **2024**, *98*, 702-13. DOI